

The Numerical Simulation and Calibration of a Shock Tube

Submitted by

Bharath Narayanan
(U076806E)

Department of Mechanical Engineering

In partial fulfillment of the requirements for the Degree of
Bachelor of Engineering

National University of Singapore

Session 2011/2012

Acknowledgement

This project has been a constant source of joy and inspiration from the start and I would like to acknowledge the people who made me love it so much.

First off, Associate Professor Vincent Tan, my supervisor who has provided me with constant guidance and has always encouraged me to be independent. Dr. Prakash Thamburaja, my external examiner, was kind enough to meet me and help solve queries after my interim presentation.

Credit is also due to Andi Haris who developed the shock tube and taught me how to use it. He has been a great sounding board for me to bounce my ideas off.

A person whose contributions I will probably never forget is Tan Long Bin. I can vouch for his genuine care for every FYP and graduate student at the Impact Mechanics Lab. Quite frankly, without him this project would not have been possible.

At the Impact Mechanics Lab, both Alvin Goh Tiong Lai and Joe Low Chee Wah have helped me immensely, from securing a desktop to helping me set up remote desktop connections. Saeid Arabnejad, Habib Pouriayeali, Kianoosh Mirandi, and Jia Shun have been fantastic people to turn to whenever my ideas came unstuck. They encouraged me to present my project to the entire lab which turned out to be the most fruitful thing I did.

The list can go on and I really cannot put into words the genuine interest and selfless help that these individuals have provided me. All I can say is thank you.

Lastly, I must thank my friends and family for supporting me through times of doubt which are inevitable in a year-long project such as this.

-Bharath Narayanan

Table of Contents

Acknowledgement.....	I
Summary	V
List of Tables	VII
List of Figures	VIII
List of Symbols	X
Chapter 1: Introduction.....	1
1.1 Objective	1
1.2 Scope.....	2
Chapter 2: Literature Review.....	3
Chapter 3: Shock Tube Experiments.....	5
3.1 Procedure	6
3.2 Results	7
Chapter 4: Modelling The Shock Tube Gas Column	9
4.1 Model and Mesh	9
4.2 Materials	10
4.3 Step.....	10
4.4 Boundary Conditions and Predefined fields	11
Chapter 5: Comparing The Simple Shock Tube Theory with Experimental Results	12
5.1 Comparison of Simulation and Theory	12

5.2 Comparison of Simulation and Experimental Results	14
Chapter 6: Effect of Viscosity on Simulation Results	17
6.1 Material Viscosity	17
6.2 Results	18
Chapter 7: Mesh Convergence.....	20
Chapter 8: Fluid Structure Interaction Model	22
8.1 Model and Mesh	22
8.2 Materials	23
8.3 Interactions	23
8.4 Boundary Conditions and Predefined Fields	24
8.5 Results	25
8.5.1 Mach number of the shock wave	26
8.5.2 Contact surface location	29
8.5.3 Frictionless contact	29
8.5.4 Element location at which data is plotted.....	30
8.5.5 Degree of correlation for driver overpressure of 88 psi	31
Chapter 9: Conclusion	33
Chapter 10: Recommendations for Future Work.....	34
References.....	36
Appendix I – Experimental Results.....	38
Appendix II – Fluid Structure Interaction Results	40
Appendix III – The Simple Shock Tube Theory.....	41

Appendix IV: Hourglass Controls	43
--	-----------

Summary

The gas column within a shock tube was modelled using the Finite Element Analysis software Abaqus/Explicit and simulations were conducted in order to reproduce the results of the Simple Shock Tube Theory. Having validated the ability of the model to accurately duplicate analytical predictions, the simulation results were then compared with the experimental results obtained using the shock tube at the Impact Mechanics Lab at NUS.

A considerable difference was observed between the theory and the actual experiments. As such, the model was improved by introducing viscosity parameters and wall boundary conditions. This resulted in a more accurate approximation of the experimental results but the difference between the simulation results and the experiments was still significant.

Moreover, it was concluded that the improved performance of the finite element model was due to the imposition of a wall boundary condition as opposed to the introduction of viscosity.

In order to reproduce the physical phenomena more accurately, a more advanced finite element model was constructed which incorporated fluid structure interaction between the gas column and the steel tube, as per the experimental setup. Initial simulations relying solely on the interaction between the gases and the tube exhibited a leakage of gases through the Lagrangian mesh which is undesirable. Repeated attempts to solve this bore no fruit.

Hence boundary conditions were assigned to the Eulerian elements that overlapped with the Lagrangian mesh in order to constrain the movement of material. This new model demonstrated an appreciable degree of conformity with the experimental results. It was also validated through a comparison with previous studies conducted by Duff.

The results of the new model showed a significant decrease in the shock wave Mach number when compared with the experimental results and the theoretical predictions. This difference is attributed to the presence of a wall boundary layer. The relatively small distance between the contact surface and the shock front is also determined to be related to the presence of this boundary layer.

It was concluded that a finite element model that incorporated fluid structure interaction, with a rough interaction between the gas column and the solid tube, provides the closest approximation to experimental results and forms the basis for future work in testing different materials' shock wave impedances.

List of Tables

Table 1: Properties of the shock tube at NUS impact mechanics lab	5
Table 2: Material properties of Air and Helium for driver pressure of 382 psi.....	10
Table 3: Mach number of shock wave and corresponding pressure difference as predicted by theory	13
Table 4: Particle velocity U_2 behind the shock wave from the simulation is used to calculate the shock wave Mach number.....	13
Table 5: Temperature dependent dynamic viscosities of air.	17
Table 6: Material properties of steel for fluid structure interaction simulations	23

List of Figures

Figure 1: Schematic diagram of the shock tube	5
Figure 2: The shock tube at NUS Impact Mechanics Lab with the Mylar diaphragm on the right and the two pressure transducers within the test chamber on the left.	6
Figure 3: Sample pressure plot taken by the two sensors at the end of the tube. Sensor A is located along the circumference and is 20 mm ahead of sensor B which is at the end of the tube.....	7
Figure 4: Model created using Abaqus/Explicit. Note the two datum plans along the tube.....	9
Figure 5: Simulation results plotted against distance at a timestamp of 0.98 ms	14
Figure 6: Pressure plot at sensor A for a driver gauge pressure of 382 psi	14
Figure 7: Pressure plot at sensor A for a driver gauge pressure of 238 psi	15
Figure 8: Pressure plot at sensor A for a driver gauge pressure of 88 psi	15
Figure 9: Effect of material viscosity on incident pressure	18
Figure 10: Effect of the imposition of a wall boundary on simulation results	19
Figure 11: Influence of element size on peak pressure.....	20
Figure 12: Influence of element size on velocity profile	21
Figure 13: Model of the gas column along with the partitioned regions comprising voids. ...	22
Figure 14: Leakage of gas through the Lagrangian mesh. The steel tube has been excluded from this viewport. Region in red is filled with voids while the gases are shown in blue.	24
Figure 15: Pressure profile for driver pressure of 382 psi.	25
Figure 16: Reflected pressure for an initial driver pressure of 382 psi.....	26
Figure 17: Location of the shock front against time gives the speed of the shock wave in metres per millisecond	27

Figure 18: View cut of the shock tube showing the laminar layer of the gas column. This is a viewport showing velocity along the direction of the tube with the red regions depicting 0 velocity.....	27
Figure 19: Pressure plots at the two sensors A and B. Timestamps are read at pressures of 0.032 bar.	28
Figure 20: The SVAVG: Pressure visualization shows the curved shock front.	29
Figure 21: Fluid structure interaction with Frictionless contact	30
Figure 22: Difference in pressure plots at the wall surface and at the centre of the tube, 20 mm away from the end of the driven section.....	30
Figure 23: Incident pressure plot for a driver pressure of 88 psi	31
Figure 24: Reflected pressure for a driver pressure of 88 psi	32

List of Symbols

γ_1 : Specific heat ratio of unperturbed air in the driven section

γ_4 : Specific heat ratio of unperturbed Helium in the driver section

U_s : Velocity of the shock wave (ms^{-1})

U_2 : Particle velocity behind the shock wave, towards the driver section (ms^{-1})

a_1 : Speed of sound in unperturbed air (ms^{-1})

a_2 : Speed of sound in unperturbed Helium (ms^{-1})

M_s : Mach number of the shock wave

P_4 : Initial driver pressure

P_1 : Initial driven pressure

T_4 : Temperature of unperturbed Helium in the driver section (K)

T_1 : Temperature of unperturbed air in the driven section (K)

R : Individual gas constant ($\text{Jkg}^{-1}\text{K}^{-1}$)

μ : Dynamic viscosity ($\text{kgm}^{-1}\text{s}^{-1}$)

ρ : Material density (kgm^{-3})

ν : Poisson's ratio

C_v : Specific Heat capacity at constant volume (JK^{-1})

Chapter 1: Introduction

The shock tube has been in use for over half a century and has helped study the behaviour of materials exposed to shock waves for use in military and civilian applications. At the Impact Mechanics Lab at the National University of Singapore, a shock tube was developed to test the shock wave attenuation characteristics of various materials.

The device comprises a long metal tube with two sections separated by a diaphragm. One of the sections, the driver section, is filled with a gas at high pressure. The other section contains ambient air. Once the pressure in the driver section is high enough to rupture the diaphragm, a shock wave is generated due to the large pressure difference between the two sections. A detailed description of the apparatus is provided by Schneider in [8].

Before the shock tube can be used to analyse the behaviour of these materials, it is necessary to calibrate the experimental apparatus using numerical methods. This will help ensure that the right parameters are being measured by the experimental setup.

Numerical simulations using commercial CFD codes have been carried out over the past decade and some institutions have even created their own modified Euler equations to accurately describe the shock wave characteristics within the shock tube.

1.1 Objective

This thesis aims to create a computational model of a shock tube and compare the results of the simulations to the actual experiments. It further seeks to obtain a refined computational model that serves to describe the experimental phenomena more accurately. The benefits of this are two-fold. An accurate computational model would allow a better understanding of the flow characteristics within the shock tube. A reliable version of such a model that is capable

of accurately reproducing experimental results will also obviate the need for multiple experimental tests.

1.2 Scope

Chapter 2 comprises a literature review where past studies that are deemed to be relevant to this thesis are outlined.

Chapter 3 describes the experimental setup that was used to obtain pressure profiles from the shock tube.

Chapter 4 covers the modelling of the shock tube gas column using Abaqus/Explicit. This section was created separately so that the work can be duplicated by another researcher as and when necessary.

Chapter 5 offers a comparison of the analytical results, obtained using the simulations, and the experimental results. Chapter 6 carries on from chapter 5, analysing the effects of the addition of viscous terms while chapter 7 describes the mesh convergence tests conducted in order to determine the appropriate element size that is to be used.

Chapter 8 describes in detail the fluid structure interaction (FSI) model that was created, including the results obtained.

The thesis concludes with chapters 9, 10 and 11 which comprise the conclusion, the future recommendations for work to be done, and the reference section respectively.

Chapter 2: Literature Review

Anderson's Simple Shock Tube Theory [6] forms one of the fundamental principles by which shock tube behaviour is studied. It provides the basic equations which are used to validate the ability of the finite element model to describe and simulate shock wave behaviour accurately.

When it comes to numerical methods, studies conducted by Carlucci et al. [2] evinced the ability of Abaqus/Explicit to accurately simulate shock wave phenomena. The results displayed a less than 0.75% discrepancy between the analytical expectations and the simulations.

In their case, the initial pressure difference between the driver and driven sections was created by modifying the driver temperature instead of the density variations used in the model covered by this thesis. Nevertheless, their study served to validate Abaqus/Explicit's ability to model shock waves as accurately as any CFD code. This is important because Abaqus/Explicit Explicit allows for the study of fluid structure interaction which obviates the need for first conducting a CFD simulation and then importing the loads into an FEA software for studying structural response. This is especially relevant to the work outlined in this thesis since fluid structure response is also analysed.

Tan et al. [4] used an Autodyn model for studying the performance of various materials in attenuating shockwaves. The importance of this paper lies in the usage of a Mie-Gruneisen equation of state in lieu of the traditional elastic-plastic model used for modelling Aluminium.

It forms a basis for comparing the performance of materials using a traditional model. The Mie-Gruneisen parameters used are also of value for the future work that needs to be done with the model outlined in this thesis.

Studies conducted by Amir et al. [5] using a two-dimensional CFD code verified the decrease in shock wave velocity due to the presence of a boundary layer and hence served to explain the deviation from theoretical predictions.

Apart from numerical simulations, Duff [1] used experimental data to study the behaviour of shock waves in long, thin shock tubes. It was found that the analytical predictions overestimated the shock wave velocity due to the inability of the theory to account for viscous effects which are prevalent in such shock tubes. He reasoned that at low driver pressures the shock tube phenomena are more accurately described by a complex pipe flow than a one dimensional shock tube theory.

The aforementioned studies helped provide a strong background for carrying out this project.

Chapter 3: Shock Tube Experiments

The shock tube at NUS uses Helium as the driver gas and ambient air in the driven section. It is closed at both ends. Once the Helium in the driver section attains enough pressure to burst the diaphragm shown in Figure 1, a shock wave is generated.

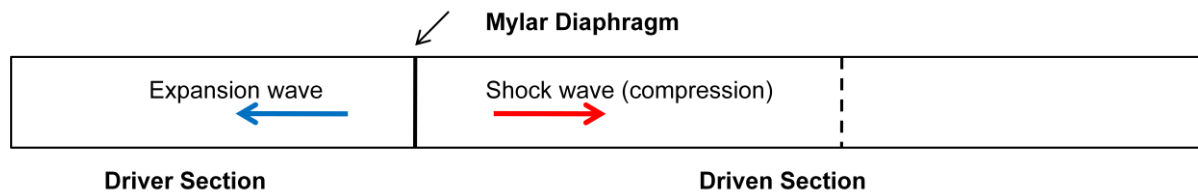


Figure 1: Schematic diagram of the shock tube

This compressive wave travels towards the driven section, increasing the temperature and pressure of the air that it encompasses. At the same time, an expansion wave travels into the driver section, reducing the pressure and temperature along the way.

Table 1: Properties of the shock tube at NUS impact mechanics lab

Length	4.6 m
Inner diameter	0.06 m
Outer diameter	0.08 m
Material	316 L stainless steel
Gases	Helium, Air
Maximum pressure	70 Bar

There are two pressure sensors at the end of the driven section that are spaced 20 mm apart. One sensor is embedded into the cylindrical wall of the tube and measures the incident pressure while the other sensor is placed at the end of the tube and measures the transmitted pressure. For the purpose of this project, only the incident pressure is of relevance.

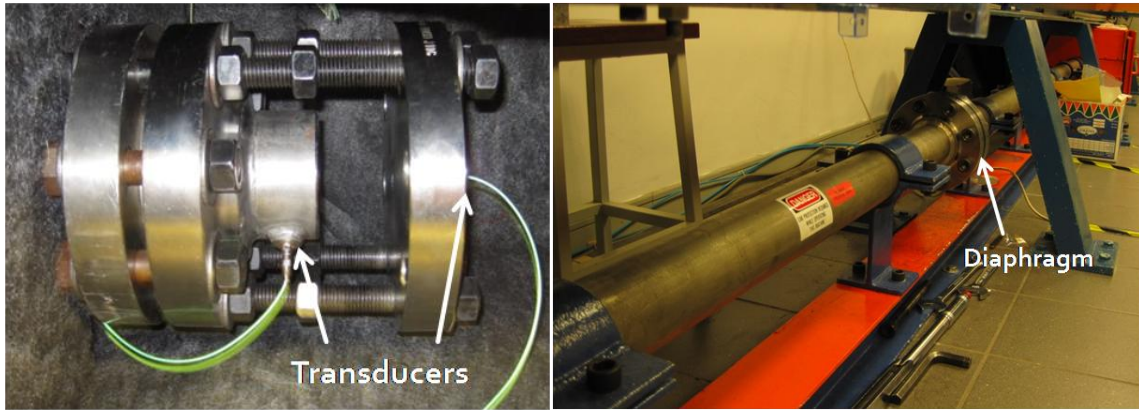


Figure 2: The shock tube at NUS Impact Mechanics Lab with the Mylar diaphragm on the right and the two pressure transducers within the test chamber on the left.

The diaphragm consists of a stack of Mylar sheets which are fitted into place using a set of bolts. The bursting pressure is varied by adding or decreasing the number of Mylar sheets. The driver section is connected to a Helium tank which supplies it with the necessary amount of gas.

3.1 Procedure

The required number of Mylar sheets is first inserted between the driver and driven sections and secured using gaskets to prevent the leakage of air. From previous experiments it was found that for a driver pressure of 10 Bar one sheet of Mylar is required and for each pressure increment of 10 Bar, 2 sheets of Mylar are to be added; i.e. for 30 Bar you would need 5 sheets of Mylar. Note that all the pressures mentioned are gauge pressures.

The gauge connected to the Helium tank measures the pressure in Bar while the gauge connected to the driver section measures it in pounds per square inch (psi). The former caps the maximum allowable pressure of Helium while the latter measures the actual pressure at which the Mylar sheets rupture.

It is important to ensure that the Mylar sheets rupture as completely as possible. For this to happen, the gas from the tank must be released steadily into the driver section. This requires a gentle opening of the valve. It is also important to ensure that all bolts and connections are secure in order to prevent any leakage of gases.

3.2 Results

Experiments were conducted at driver pressures of 88 psi, 238 psi and 382 psi. Pressures higher than these were not tested since the operating pressure for material testing is only about 90 psi. This is deemed to be sufficient enough to measure the attenuation of amplification of a pressure wave. Also, if the bursting pressure is increased and the specimen to be tested is amplifying in nature, there is a risk that the pressure transducer might be damaged.

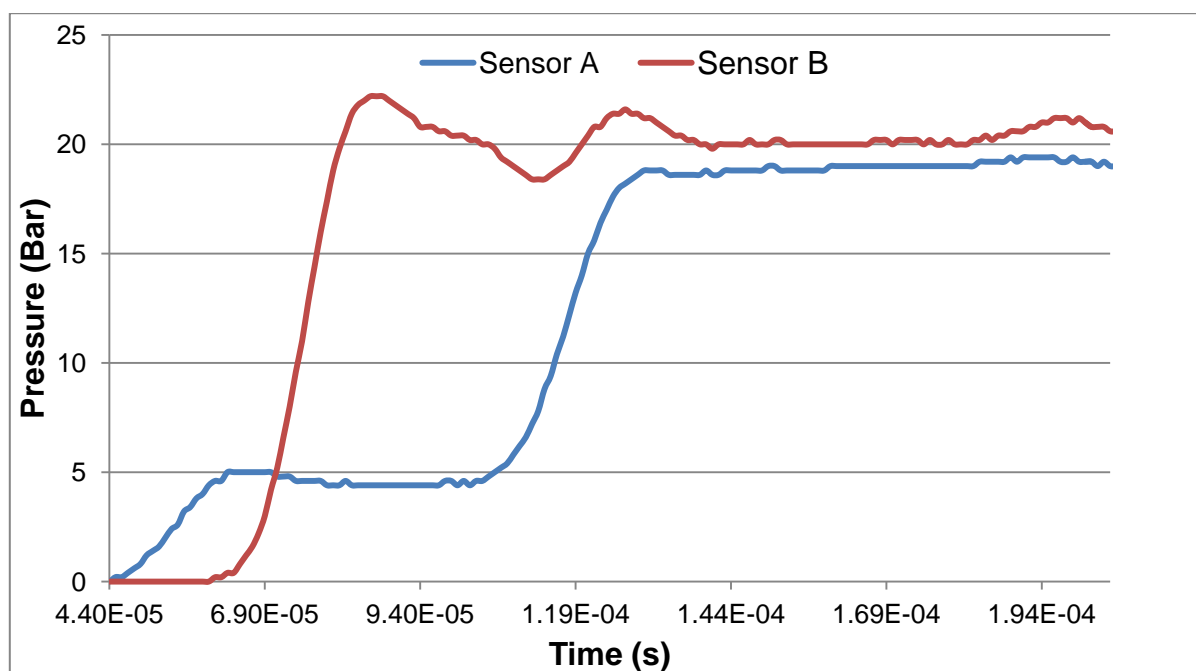


Figure 3: Sample pressure plot taken by the two sensors at the end of the tube. Sensor A is located along the circumference and is 20 mm ahead of sensor B which is at the end of the tube.

The two sensors originally provide a plot of voltage against time. This is converted into a pressure plot by multiplying the voltage by a factor of 5 (the gauge factor) and then zeroing the pressure.

The larger peak for sensor B, as shown in figure 2, is attributed to the fact that it includes the reflected part of the wave as well. This is because the sensor is located at the end of the tube, resulting in an instantaneous superposition of the incident and reflected pressure waves.

Chapter 4: Modelling The Shock Tube Gas Column

4.1 Model and Mesh

Abaqus CAE 6.10 is used to create an idealized version of the shock tube for simulation purposes. Only the gaseous column is modelled without accounting for the surrounding steel tube. A 4.6m long tube, with a diameter of 0.06m, is extruded. Two datum planes are created; one at the end of the driven section and one 3.3m away from the driven end. Using the datum planes, a partition is created in order to assign different material properties to each partitioned cell.

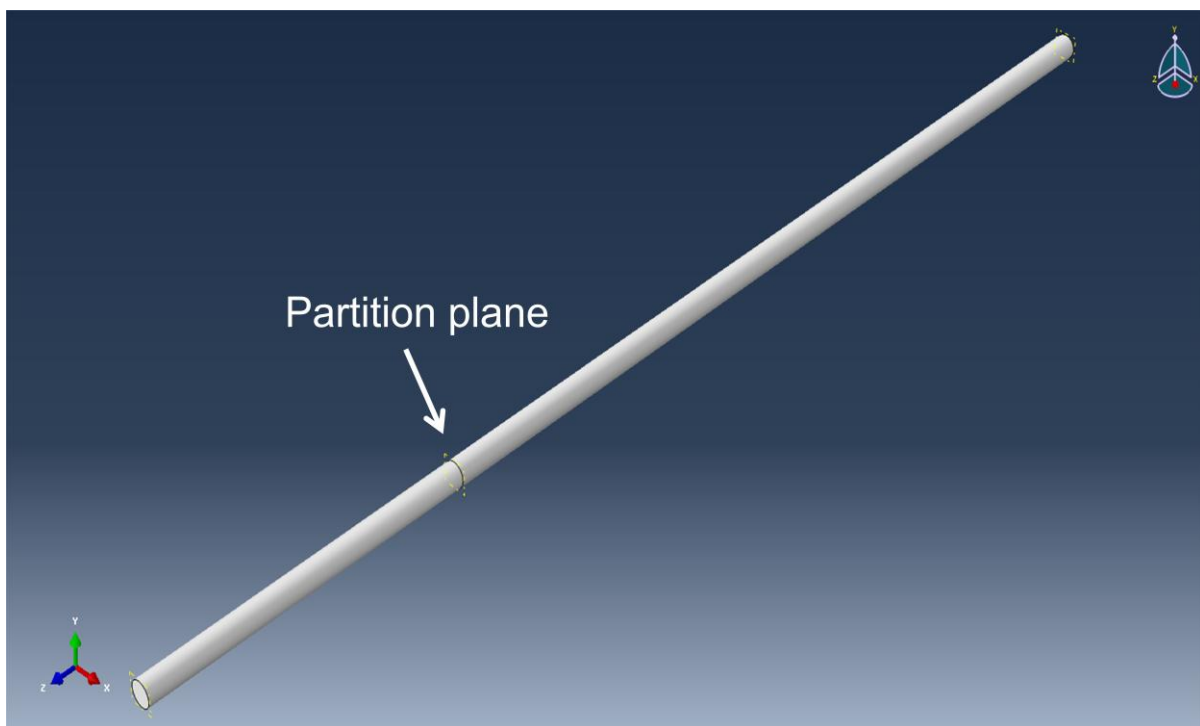


Figure 4: Model created using Abaqus/Explicit. Note the two datum plans along the tube.

An EC3D8R 8-node Eulerian brick element with reduced integration is used to model the gas combination in order to be able to observe the motion of the gases within the gas column. A seed size of 5 mm is used. The default hourglass control for the EC3D8R is viscous. While the default settings are good for modelling solid behaviour, they could affect the results of

fluid behaviour undesirably [10][11]. Hence all three parameters; displacement hourglass, linear bulk viscosity, and quadratic bulk viscosity are turned off. A detailed description of the parameters is given in Appendix IV along with the reason for their exclusion.

4.2 Materials

Helium and air are modelled using the ideal gas equation of state. The relevant parameters are listed in table 2.

Table 2: Material properties of Air and Helium for 382 psi driver pressure (room temperature).

	Helium	Air
Density (kgm^{-3})	4.382	1.177
Ambient Pressure (Pa)	0	0
Gas constant ($\text{Jkg}^{-1}\text{K}^{-1}$)	2077	287
Specific Heat (JK^{-1})	3120	716

4.3 Step

A single explicit step is used with a step time of 4.5 to 6.5 ms depending on the intensity of the generated shockwave. The following field outputs are chosen for analysis:

- **SVAVG:** This consists of the pressure terms and Mises stress terms
- **V:** Translational and rotational velocities
- **EVF:** Void and material volume fractions
- **TEMP:** Individual element temperature
- **DENSITYAVG:** Volume average material density

The field output parameters are calculated at even intervals at 3000 such intervals.

4.4 Boundary Conditions and Predefined fields

Zero velocity boundary conditions are applied to both ends of the tube in order to simulate the presence of a wall or barrier.

The ‘predefined field’ dialogue box is used to apply the two materials, Helium and air, to the driver and driven regions of the tube respectively. The dialogue box is also used to assign the ambient temperature of 300 Kelvin to the entire tube. This is necessary for the software to compute the initial pressure of the Helium and air sections using the ideal gas equation of state.

The jobs are run on multiple cores ranging from 4 to 12. Double precision is used for both the analysis and the packager.

Chapter 5: Comparing The Simple Shock Tube Theory with Experimental Results

In order to simulate the Simple Shock Tube Theory, the assumptions of the theory are inputted into Abaqus/Explicit. This involves a planar motion of the gases i.e. velocity components in the radial directions throughout the model are set to zero. No material viscosity is inputted. In addition, no wall boundary is imposed on the gas column.

5.1 Comparison of Simulation and Theory

Before comparing the results of the theory and the experiments, it was necessary to ensure that the software could accurately describe and follow the theoretical shock wave profile.

Two parameters were deemed to be important, the Mach number of the shock wave and the pressure profile along the shock tube.

The relevant equations are outlined below and are obtained from the Simple Shock Tube Theory [8].

$$\frac{p_4}{p_1} = \frac{2\gamma_1 M_s^2 - (\gamma_1 - 1)}{\gamma_1 + 1} \left[1 - \frac{\gamma_4 - 1}{\gamma_1 + 1} \frac{a_1}{a_4} \left(M_s - \frac{1}{M_s} \right) \right]^{-2\gamma_4 / (\gamma_4 - 1)} \dots\dots\dots(1)$$

Equation 1 relates the initial driver to driven pressure ratio (p_4/p_1) to the Mach number of the shock wave (M_s). Table 3 uses the equation to tabulate a series of pressure ratios and the corresponding shock wave Mach numbers. Equation 2 relates the shock wave Mach number to the particle velocity behind the shock wave (U_2). This is used to determine the Mach number of the shock wave from the simulations as depicted in table 4.

$$U_2 = \frac{2a_1}{\gamma_1 + 1} \left[M_s - \frac{1}{M_s} \right] \dots\dots\dots(2)$$

Table 3: Mach number of shock wave and corresponding pressure difference as predicted by theory

M_s	$\gamma^2 * M_s^2$	$F7-\gamma-1$	$G7/\gamma+1$	$M_s-(1/M_s)$	p_4/p_1
1.95	10.647	10.247	4.269583333	1.437179487	8.85139
2	11.2	10.8	4.5	1.5	9.65568
2.01	11.31228	10.91228	4.546783333	1.512487562	9.8233
2.02	11.42512	11.02512	4.5938	1.524950495	9.99324
2.025	11.48175	11.08175	4.617395833	1.53117284	10.0791

Table 4: Particle velocity U_2 behind the shock wave from the simulation is used to calculate the shock wave Mach number

U_2 (ms^{-1})	ρ_2	ρ_1	U_s	T_s	γ	R	a_s	M_s
443	3.2551	1.17709	693.938	497	1.4	287	347.189	1.99873
448	3.26011	1.177	701.129	320	1.4	287	347.189	2.01945

As shown in table 3, and verified by the Gas Dynamics Calculator [7], for an initial pressure ratio of 10, the predicted shock wave Mach number is approximately 2.02. The simulation results at two different timestamps yield Mach numbers of 1.99 and 2.01 respectively resulting in a difference of less than 1%. In addition to verifying the Mach number, the pressure and temperature profiles along the length of the tube were also verified. Appendix III provides a glimpse of the theoretical distance time graphs.

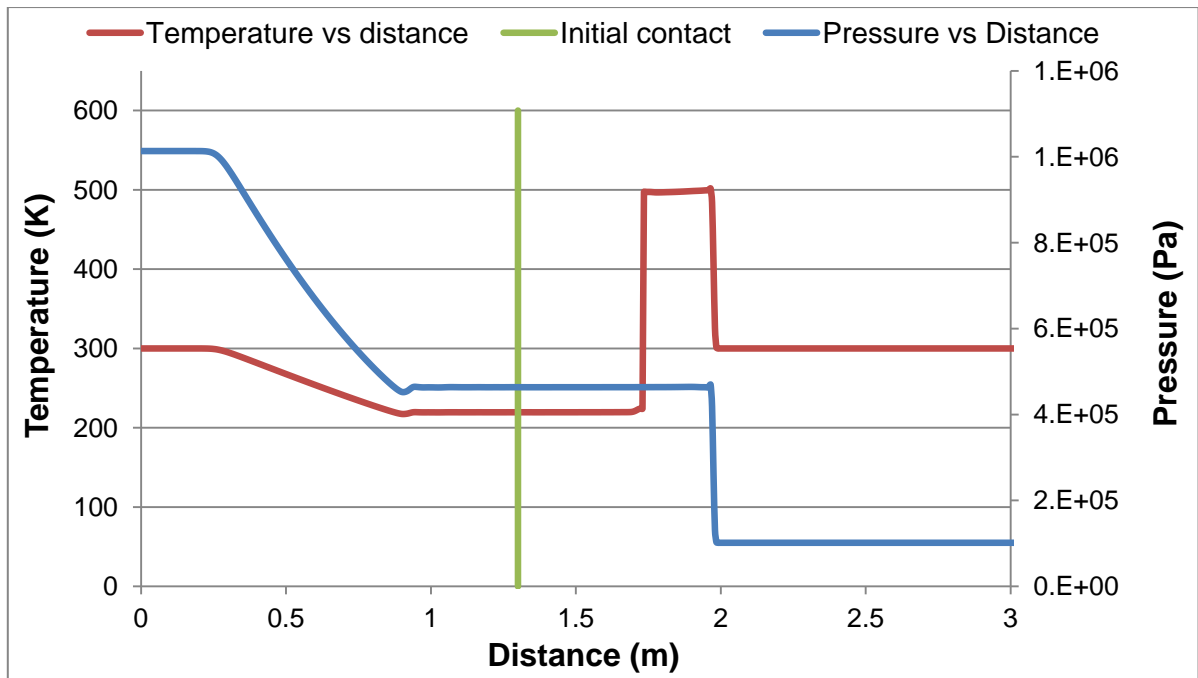


Figure 5: Simulation results plotted against distance at a timestamp of 0.98 ms

5.2 Comparison of Simulation and Experimental Results

Following the above verification exercise, the simulation results were compared with experimental results at driver pressures of 382 psi, 238 psi and 88 psi.

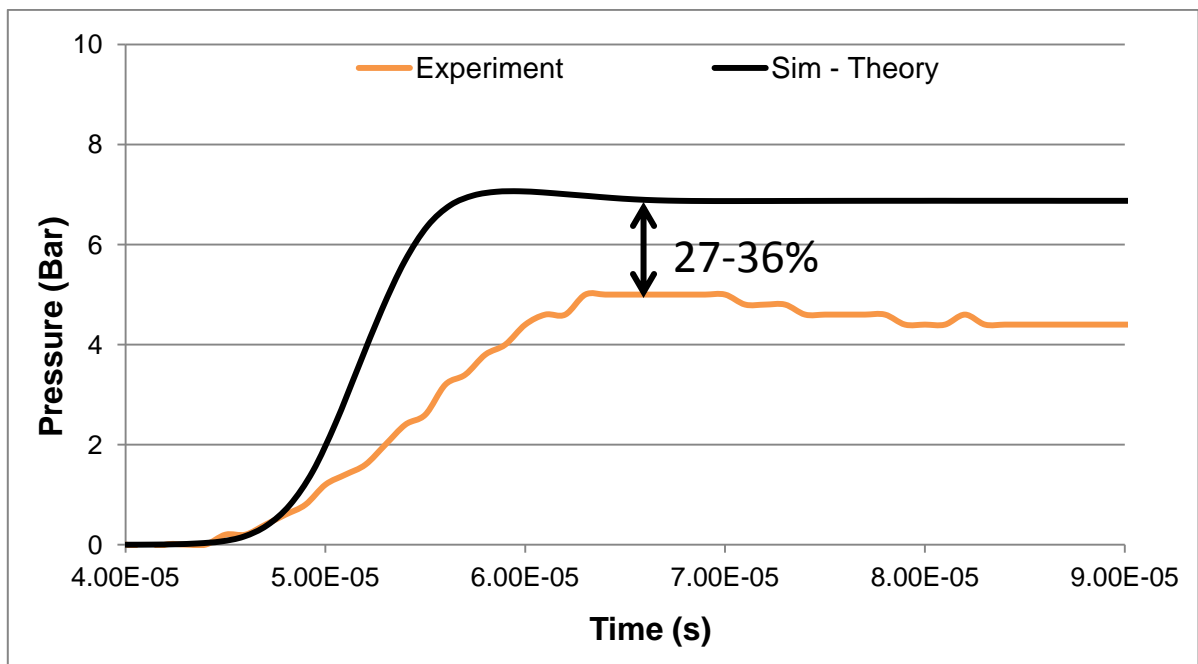


Figure 6: Pressure plot at sensor A for a driver gauge pressure of 382 psi

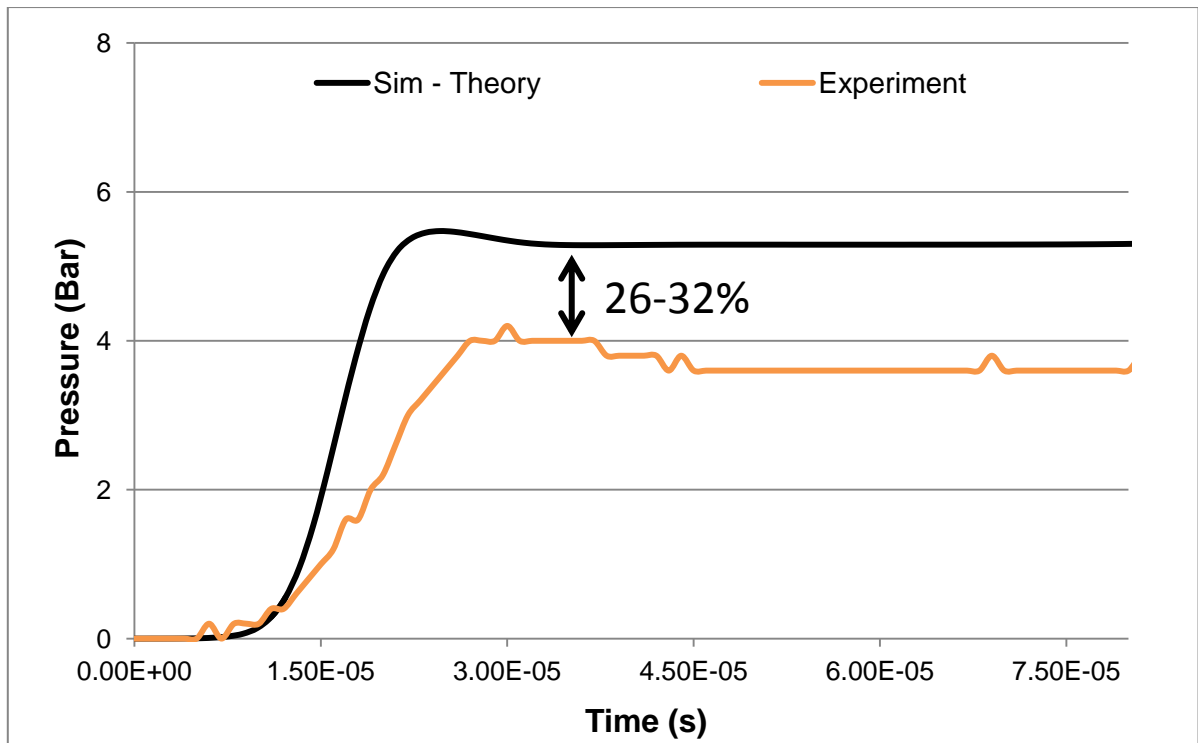


Figure 7: Pressure plot at sensor A for a driver gauge pressure of 238 psi

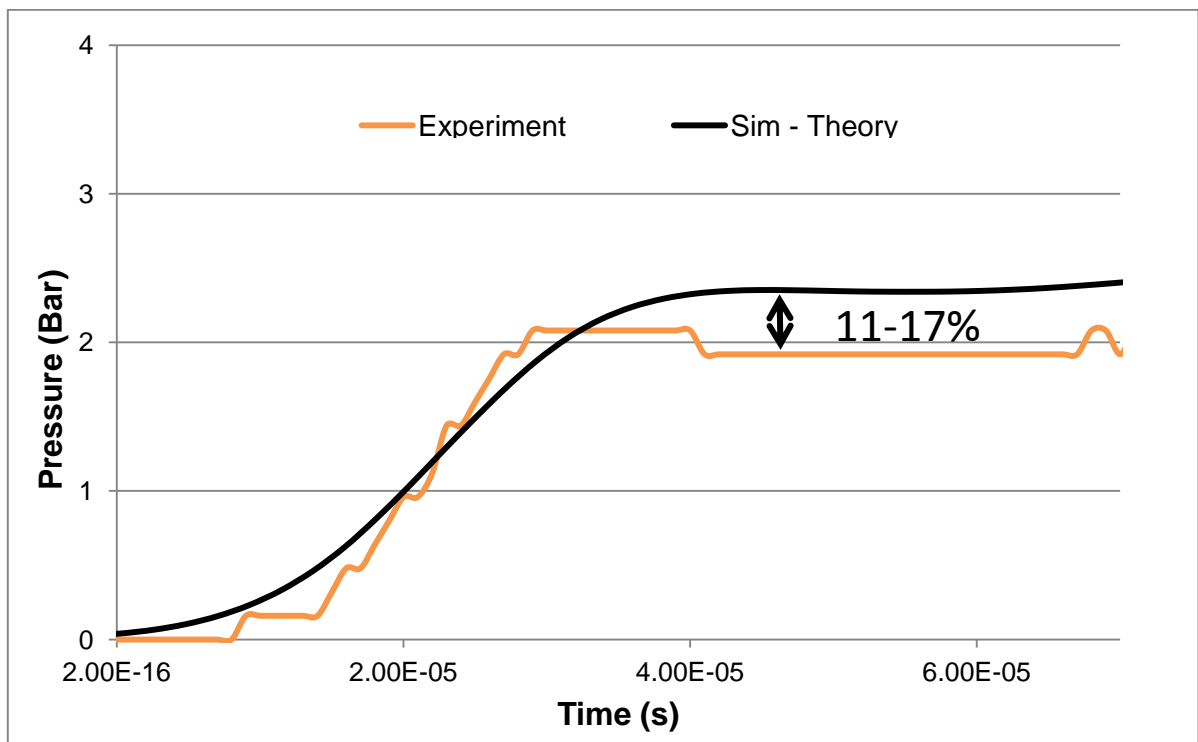


Figure 8: Pressure plot at sensor A for a driver gauge pressure of 88 psi

The graphs highlight a significant over-prediction by the theory when compared with the experimental results. The difference increases with increasing driver pressure, from about 10% for the 88 psi driver pressure to 30% for the 382 psi driver pressure. Of particular interest is the 88 psi region since this is the pressure at which most experimental tests are conducted.

Chapter 6: Effect of Viscosity on Simulation Results

The simulations listed in the previous sections served to highlight the discrepancy between theory and actual experiments. In order to ameliorate this difference, material viscosity terms were taken into account. For all simulations with viscosity, a no slip wall boundary condition was created by assigning all velocity components at the surface a value of zero.

6.1 Material Viscosity

To study the effects of fluid viscosity on the shock wave, material viscosity terms were added to the properties of both gases. Temperature dependent dynamic viscosity coefficients were readily available for air. However, a single temperature-independent viscosity parameter of $1.9\text{E-}005 \text{ kgm}^{-1}\text{s}^{-1}$ was inputted for Helium.

Table 5: Temperature dependent dynamic viscosities of air.

Viscosity ($\text{kgm}^{-1}\text{s}^{-1}$)	Temperature (K)
1.488E-005	250
1.983E-005	300
2.075E-005	350
2.286E-005	400
2.484E-005	450
2.671E-005	500

6.2 Results

Figure 8 shows the reduction in peak pressure values upon the addition of viscosity terms.

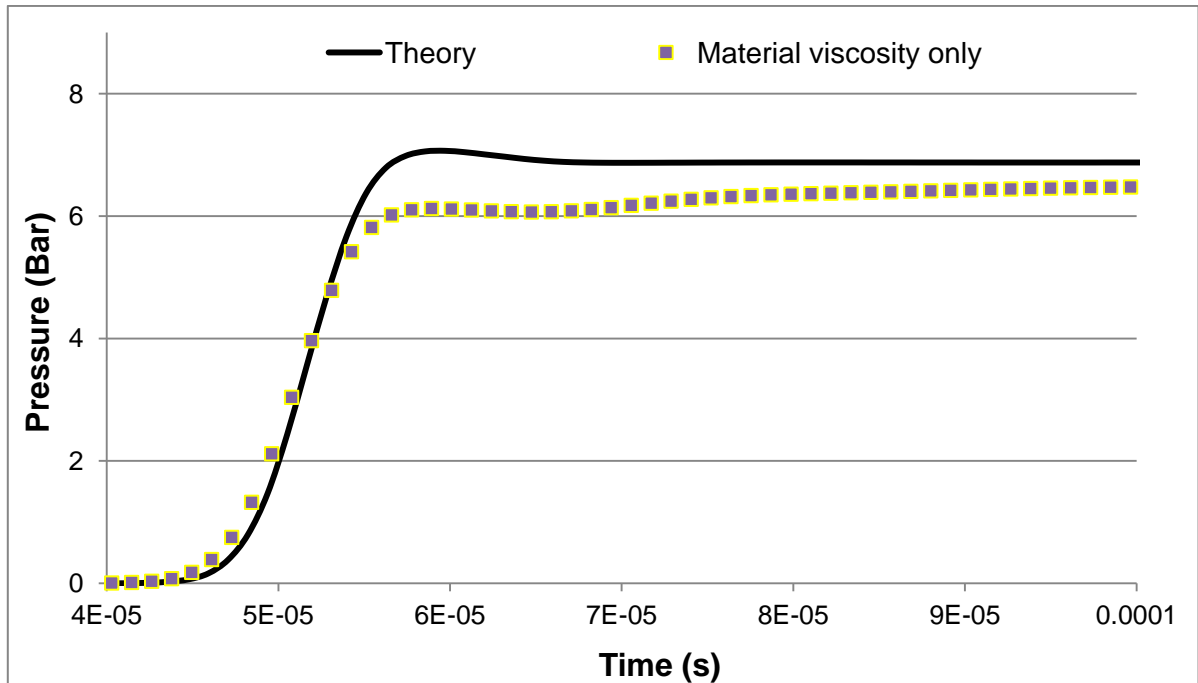


Figure 9: Effect of material viscosity on incident pressure

However, considering that a no slip condition was imposed on the wall boundary for the viscous case, it was imperative to verify whether the reduction in pressure in the simulation was due to the user inputted viscosity terms or the imposition of a wall boundary condition.

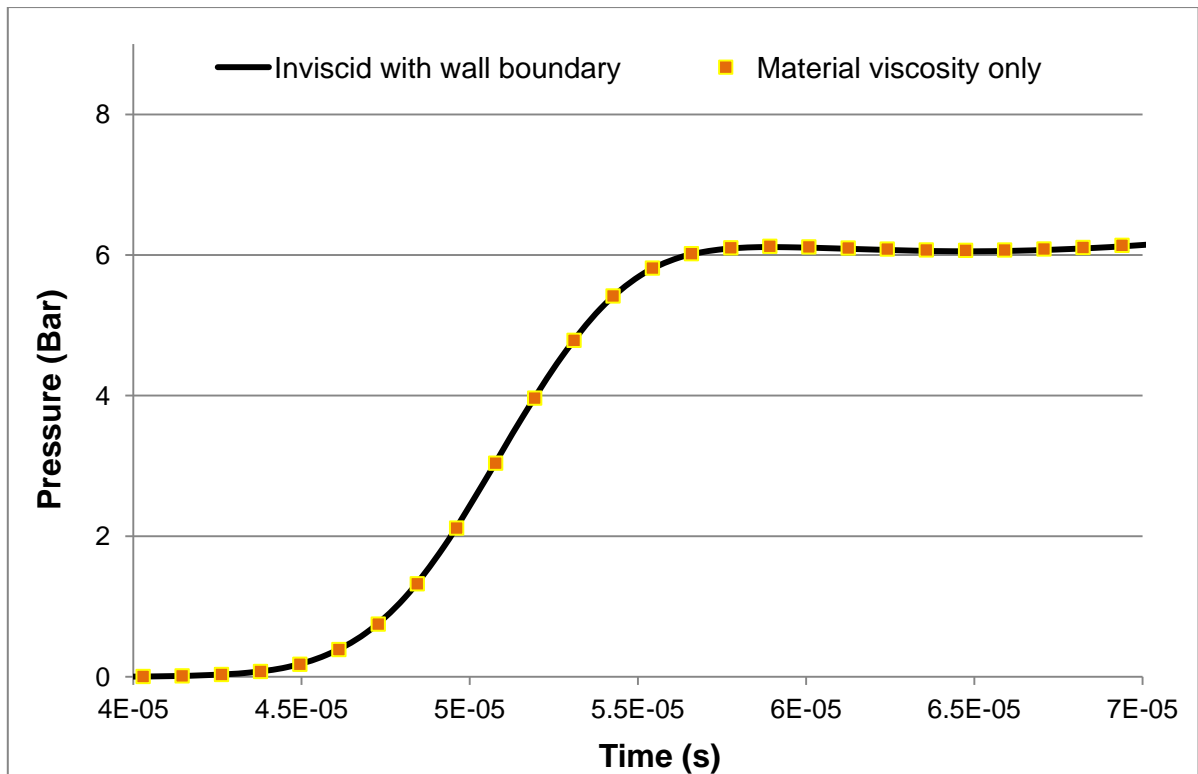


Figure 10: Effect of the imposition of a wall boundary on simulation results

The almost identical pressure curves shown in figure 9 helped eliminate user inputted viscosity as a deciding factor in the reduction in pressure and attributed it to the imposition of a wall boundary condition. Note that this does not mean that there are no shearing forces within the tube. It just eliminates the need for inputting material viscosity terms.

Chapter 7: Mesh Convergence

The accuracy of a simulation is greatly affected by the size of each individual element used. As such it is important to conduct a mesh convergence study. In essence this involves running the same simulation under various mesh sizes and finding an element size that combines accuracy with computational efficiency.

As such, inviscid simulations were run at mesh sizes of 0.5, 1, and 2 cm.

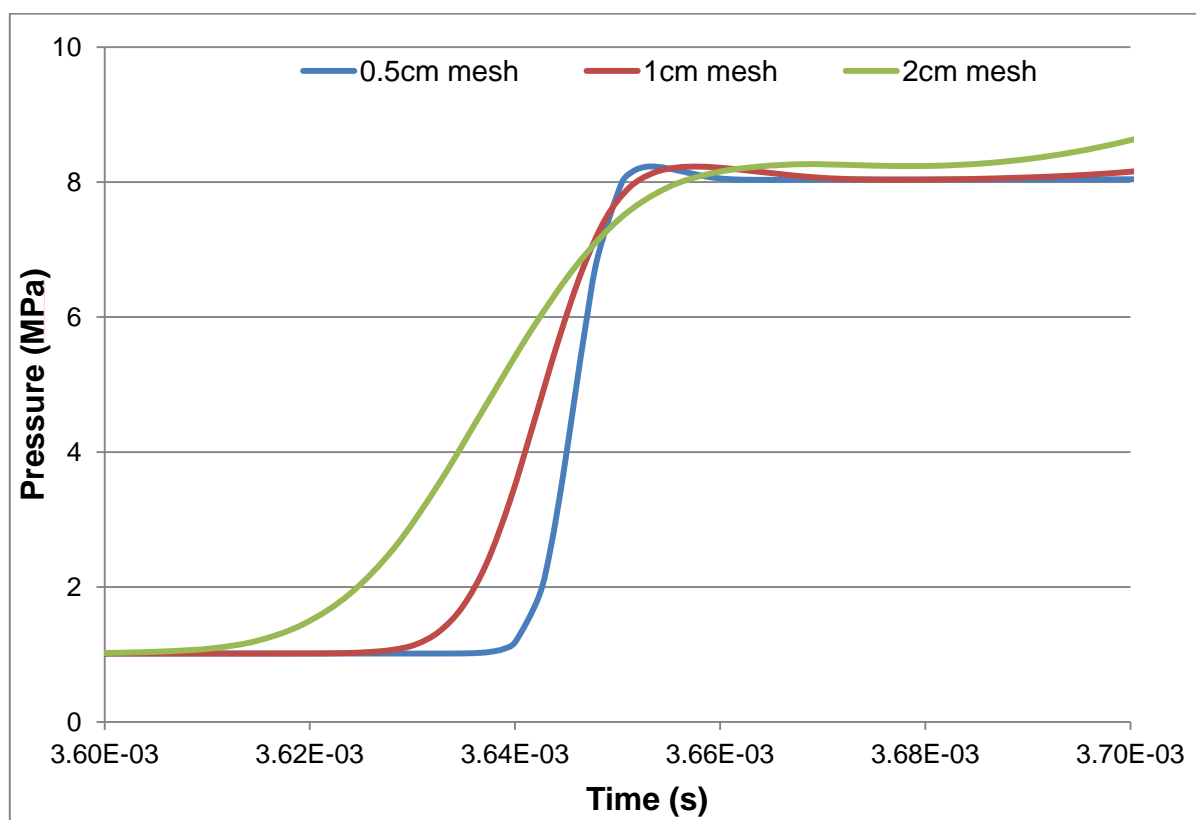


Figure 11: Influence of element size on peak pressure

It is observed that refining the mesh increases the gradient of the pressure profile while not affecting the stable magnitude.

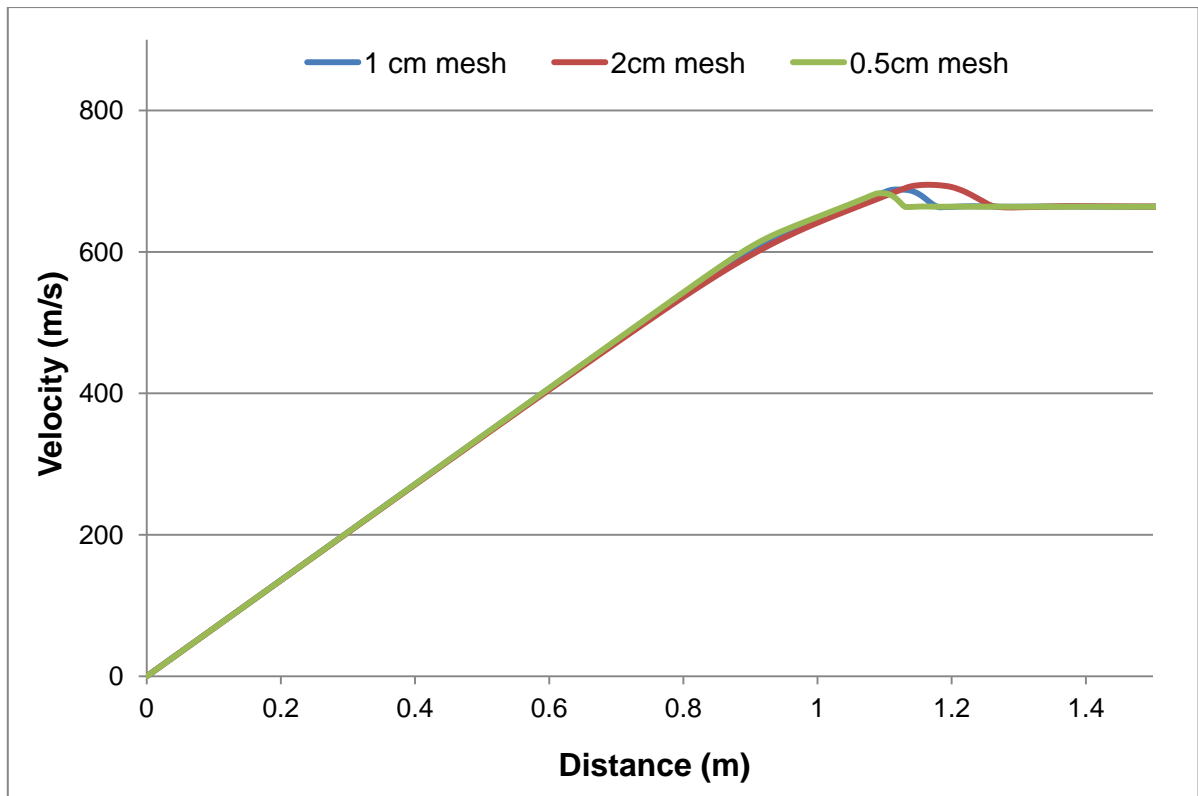


Figure 12: Influence of element size on velocity profile

For the velocity and temperature profiles, a decrease in element size reduces the magnitude and length of the overshoot as shown in figure 13. However, as with the pressure profile, the stable magnitudes for velocity and temperature are unaffected.

Chapter 8: Fluid Structure Interaction Model

In order to study the effects of fluid structure interaction on the shock wave properties, an analysis was conducted using the available Coupled Eulerian-Lagrangian methodology in Abaqus/Explicit.

8.1 Model and Mesh

The solid tube was modelled using the solid extrude option. It is 4.7m long and 0.08m in external diameter. The interior hollow shell is 0.06m in diameter and 4.6m in length. In addition to the modelling of the tube, the Eulerian mesh representing the gaseous mixture was extended in order to overlap with the Lagrangian mesh. This is done in order to ensure that forces and stresses are transmitted accurately between the two mesh types.

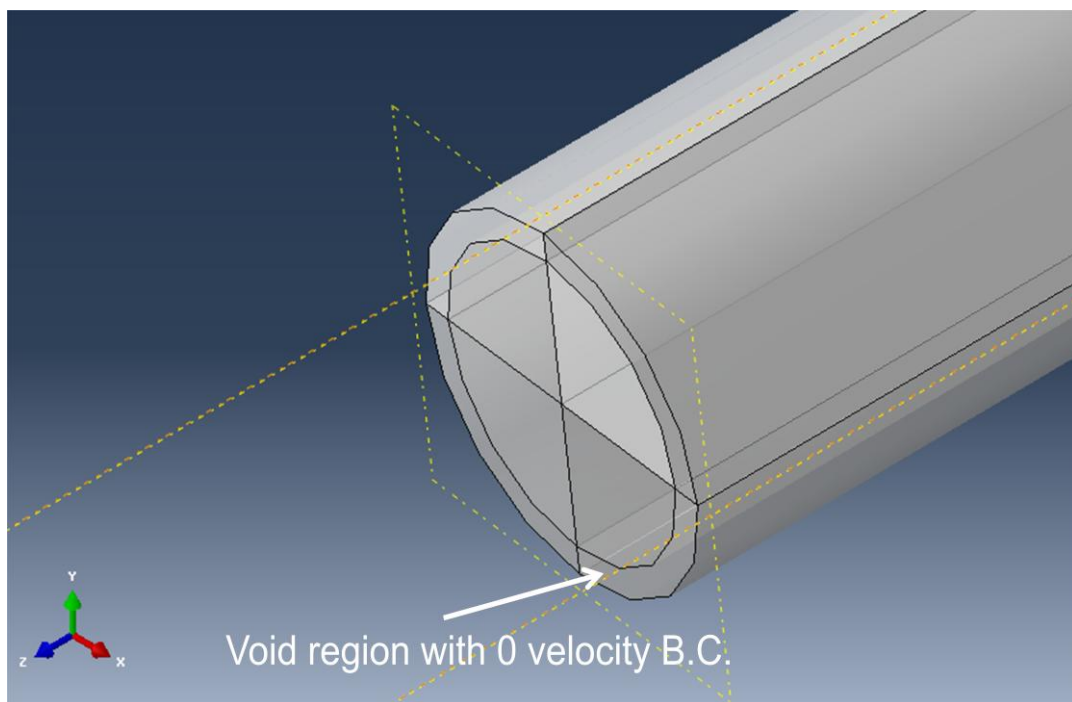


Figure 13: Model of the gas column along with the partitioned regions comprising voids.

For the solid tube, a standard C3D8R brick element was used. Care was taken to ensure that the element size of the Eulerian mesh was smaller than that of the Lagrangian mesh. This is essential in order to ensure that the Eulerian node recognizes the presence of an overlapping Lagrangian element.

After the mesh convergence studies were conducted, it was decided that a 5 mm Eulerian mesh would be best suited considering the accuracy required and the space and time constraints faced. Consequently, a 1 cm Lagrangian mesh was used for the steel tube.

8.2 Materials

In addition to the two gases described earlier, steel was added as another material. The shock tube at NUS uses 316L stainless steel and hence the following properties were inputted.

Table 6: Material properties of steel for fluid structure interaction simulations

Density (kgm^{-3})	8000
Young's Modulus (GPa)	193
Poisson's Ratio	0.33

8.3 Interactions

A general ‘*all with self’ contact was setup. The interaction property involved both ‘normal’ and ‘tangential’ contact. Normal contact was defined as ‘hard’ while either ‘frictionless’ or ‘rough’ was used to define the tangential contact. Rough contact constrains the overlapping Eulerian and Lagrangian nodes, creating a no slip condition.

In addition to the field output parameters specified for the gas column simulations, ‘S: solid stresses’ were also requested in order to study the forces experienced by the tube itself.

8.4 Boundary Conditions and Predefined Fields

In trial simulations, the Eulerian elements that overlapped with the Lagrangian mesh were filled with voids. No boundary conditions were prescribed and the material interaction was described by the interaction properties alone. It was assumed that this would lead to a sufficiently accurate simulation of the physical interaction between the tube and the gas mixture.

The simulations displayed a systemic leakage of gases into the void region occupied by the steel tube, as depicted in Figure 15. The Simulia lectures on fluid structure interaction [9] acknowledged the presence of this leakage and recommended a filleting of Lagrangian edges and an Eulerian element size at least three to four times smaller than the Lagrangian element. Despite the enforcement of these prescribed solutions, the leakage persisted.

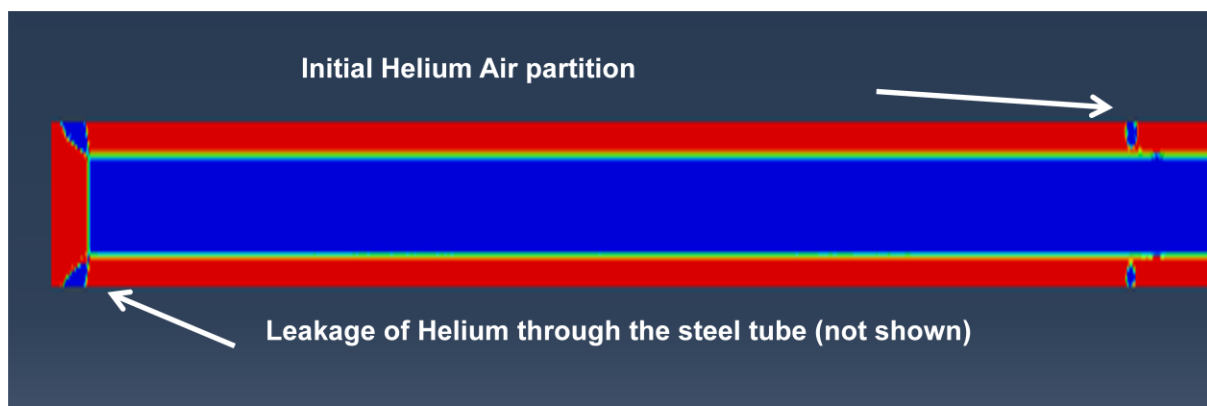


Figure 14: Leakage of gas through the Lagrangian mesh. The steel tube has been excluded from this viewport. Region in red is filled with voids while the gases are shown in blue.

In order to circumvent this problem, a zero velocity boundary condition was assigned to the overlapping void region in order to prevent material movement. However this merely resulted in results analogous to the ones obtained using the gas column model outlined in chapter 4 since the stresses are prevented from being completely transferred to the steel tube.

Considering the prevalent issues, it was decided to make the Eulerian elements filled with material overlap slightly with the Lagrangian mesh in order to effectively transmit forces and stresses. Although this is physically unrealistic, it would provide a rough estimate of the effect of fluid structure interaction on the pressure profile.

For the fluid structure interaction simulations, jobs were run on 12 cores with double precision for both the analysis and the packager.

8.5 Results

The figure below clearly indicates a drastic decrease in incident pressure discrepancy between the simulations and the experiments. It is interesting to note that even the reflected portion of the pressure profile tallies with the experimental profile as shown in figure 16. Note that the pressure plot was tapped from an element near the wall. The significance of this is outlined in chapter 8.5.4.

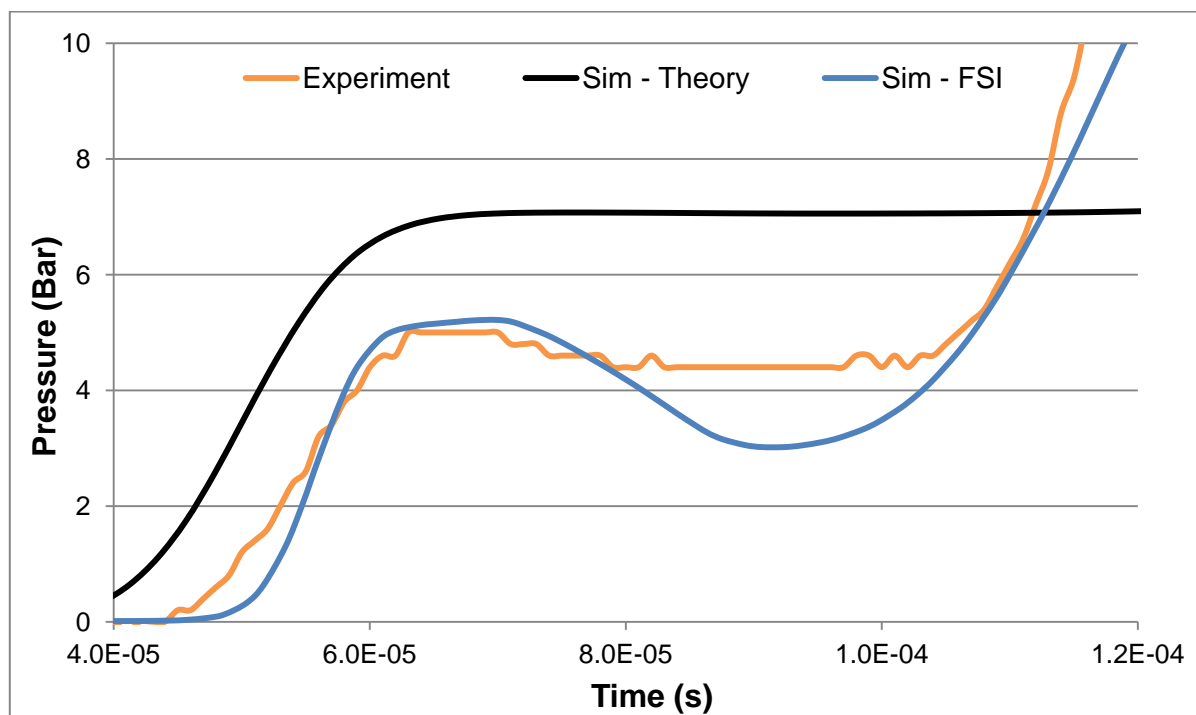


Figure 15: Pressure profile for driver pressure of 382 psi.

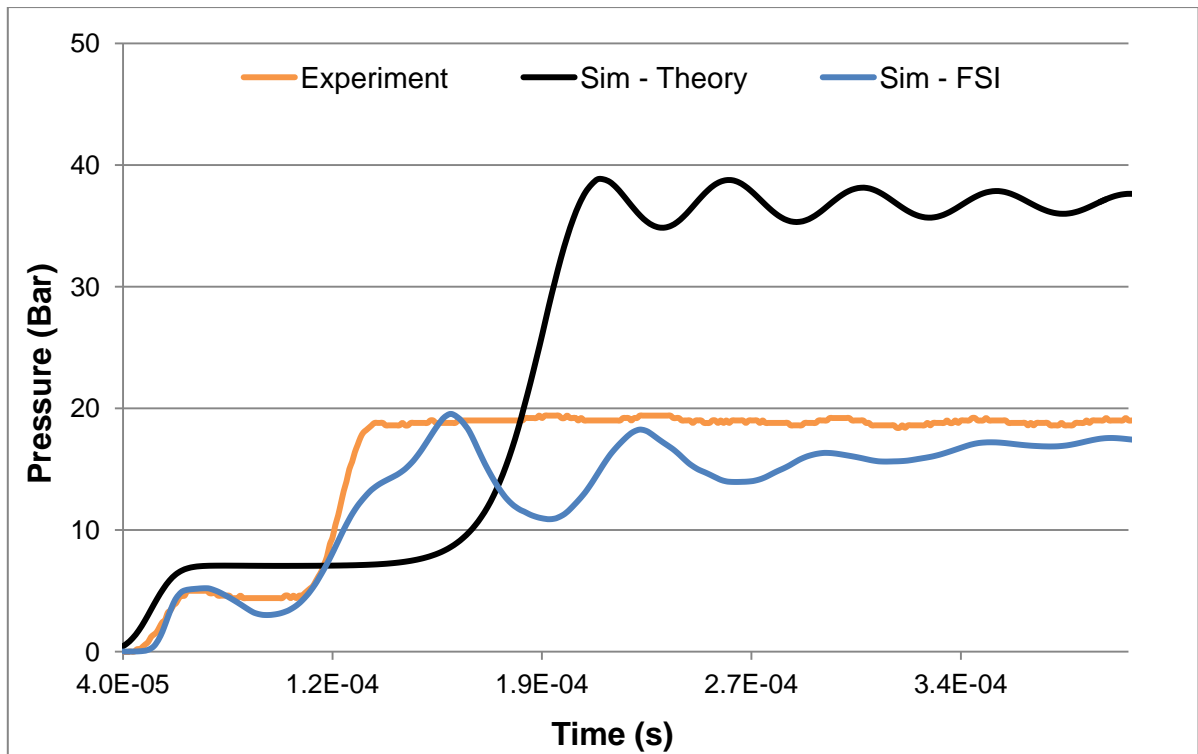


Figure 16: Reflected pressure for an initial driver pressure of 382 psi.

8.5.1 Mach number of the shock wave

The analytical equations predict a Mach number of 2.654 for an initial driver to driven pressure ratio of 26.99. In order to roughly estimate the velocity of the shock wave from the simulation, the position of the wave front is noted at 5 different time stamps. The slope of the corresponding x-t graph provides the simulation shock wave speed and thus the Mach number, which is found to be 2.25.

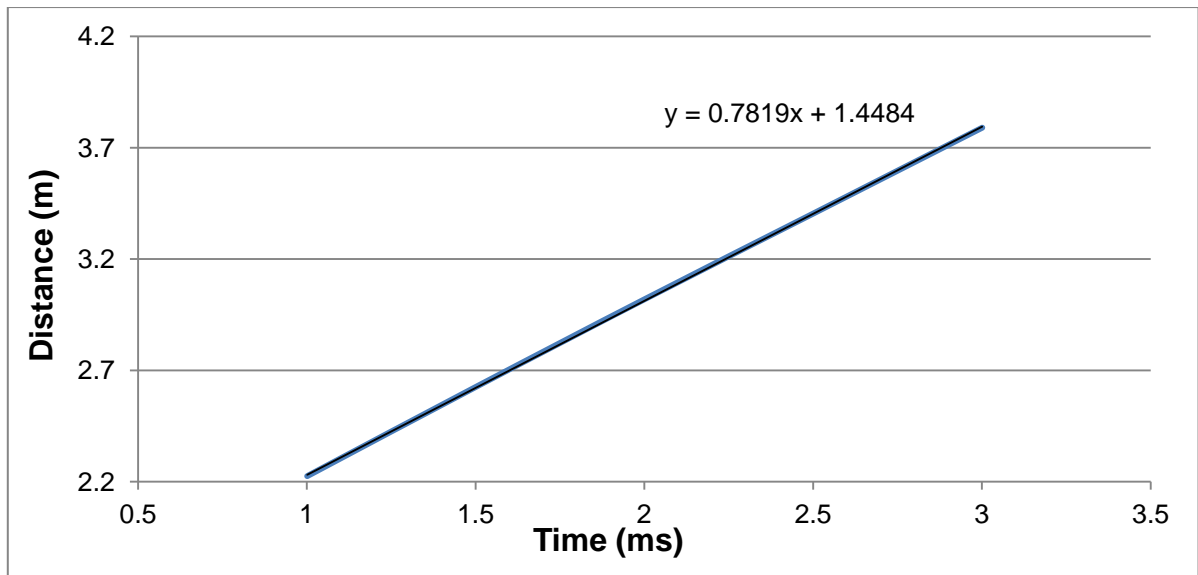


Figure 17: Location of the shock front against time gives the speed of the shock wave in metres per millisecond

The difference of 15% is due to the laminar boundary layer that is formed on the inner surface of the tube.

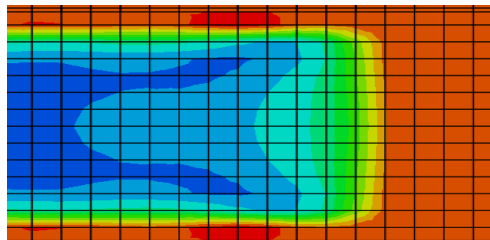


Figure 18: View cut of the shock tube showing the laminar layer of the gas column. This is a viewport showing velocity along the direction of the tube with the red regions depicting 0 velocity.

This observation tallies with Duff's assertion that in long shock tubes, the development of a laminar wall boundary layer behind the shock wave results in a reduction in Mach number when compared with theoretical predictions [1].

In the experiment, the shock wave velocity was calculated by noting the timestamp at which the two sensors start picking up the incoming shock wave. The distance between the two

sensors is known to be 20 mm; the velocity of the shockwave is easily calculated. However, it must be noted that this value is a crude approximation.

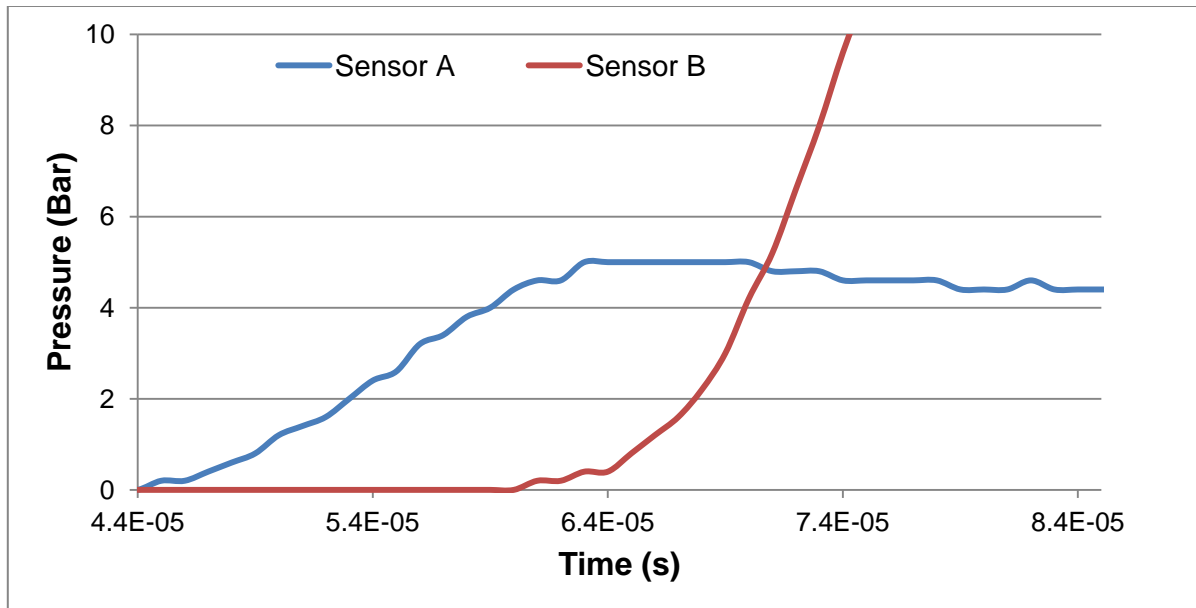


Figure 19: Pressure plots at the two sensors A and B. Timestamps are read at pressures of 0.032 bar.

Using the above graph, the velocity of the shock wave was found to be 1250 ms^{-1} which is higher than the values obtained from the simulation and theory.

This difference can be attributed to the curved surface of the shock front. This is due to the fact that at the moment when sensor A (along the wall surface) picks up the shock front, the portion of the shock front at the centre of the tube has already progressed past the sensor. The second sensor, being mounted at the centre of the tube, records the pressure value of this central part of the shock front. This results in a miscalculation of the actual distance travelled by the shock wave between the two gauges.

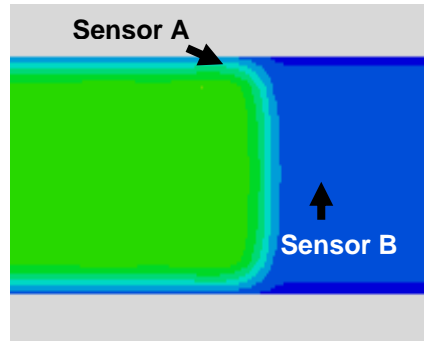


Figure 20: The SVAVG: Pressure visualization shows the curved shock front.

In order to verify this assumption using the simulation, pressure plots were tapped from an element near the wall, four elements away from the end of the tube; and from an element at the central end of the tube. The method used to obtain the shock wave velocity from experimental data was used to determine the shock wave velocity of the simulation. This yielded a velocity of 1100ms^{-1} , which is approximately the same value that was calculated using the experimental data.

8.5.2 Contact surface location

According to theory, the contact surface between Helium and Air moves at a lower velocity than the shock front, creating a distance between the two. However the contact surface in the FSI model moves at almost the same velocity as the shock front. This decrease is attributed by Duff to the presence of the laminar boundary layer observed in the simulation [1].

8.5.3 Frictionless contact

Frictionless contact was used in some simulations in order to study the effect of a no slip condition. As shown in figure 21, the frictionless contact definition results in an incident pressure profile that almost matches the theoretical profile. However, the reflected profile is markedly lower. This can be attributed to the transfer of energy and stresses at the end of the steel tube.

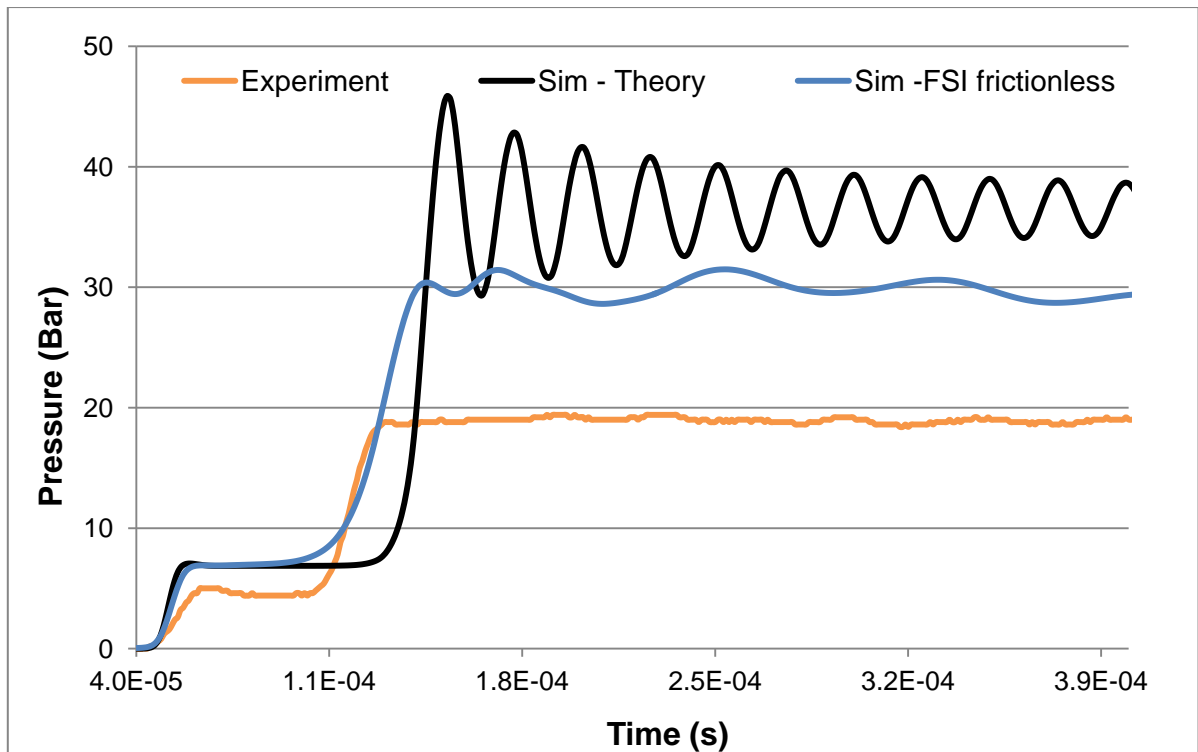


Figure 21: Fluid structure interaction with Frictionless contact

8.5.4 Element location at which data is plotted

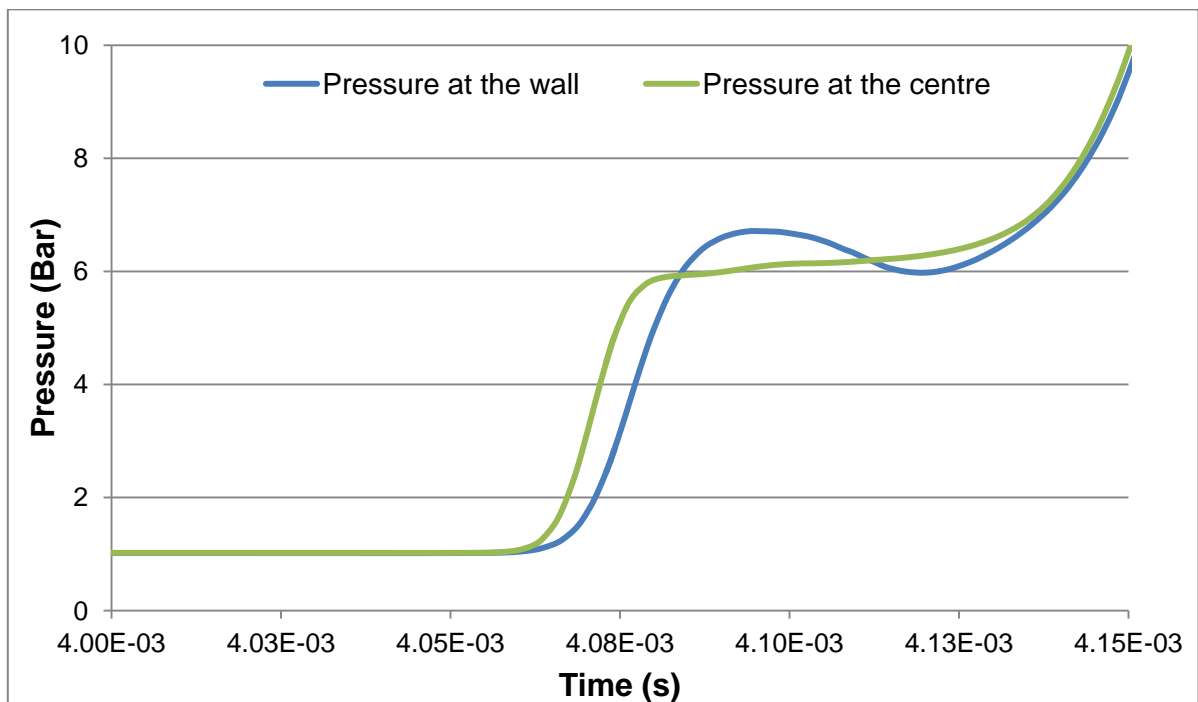


Figure 22: Difference in pressure plots at the wall surface and at the centre of the tube, 20 mm away from the end of the driven section

The pressure plots in figure 22 are taken at two different locations; one at the centre of the tube and one along the circumference. Both are tapped at a distance of 20 mm away from the end of the driven section.

The near wall pressure reading shows a distinct overshoot in the incident pressure region. The overshoot becomes more significant as the driver overpressure decreases to about 88 psi.

8.5.5 Degree of correlation for driver overpressure of 88 psi

While the fluid structure interaction model is seen to form a better approximation of the experimental setup at a driver pressure of 382 psi, it is also important to study the degree of conformance at a pressure of 88 psi.

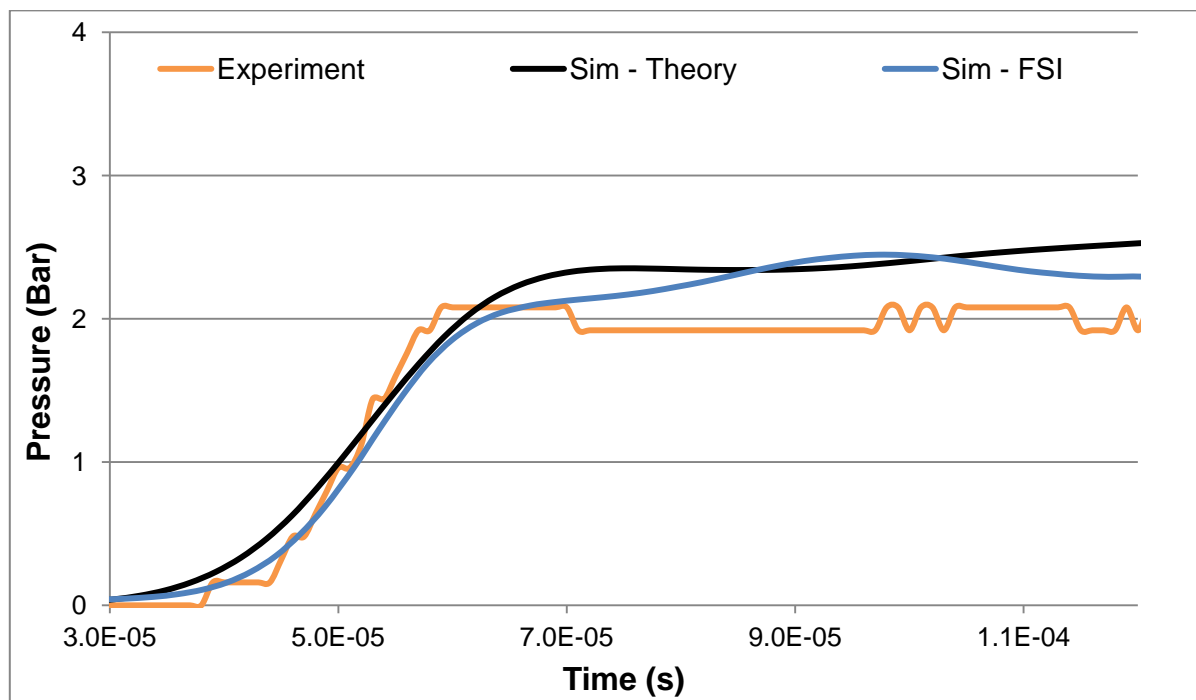


Figure 23: Incident pressure plot for a driver pressure of 88 psi

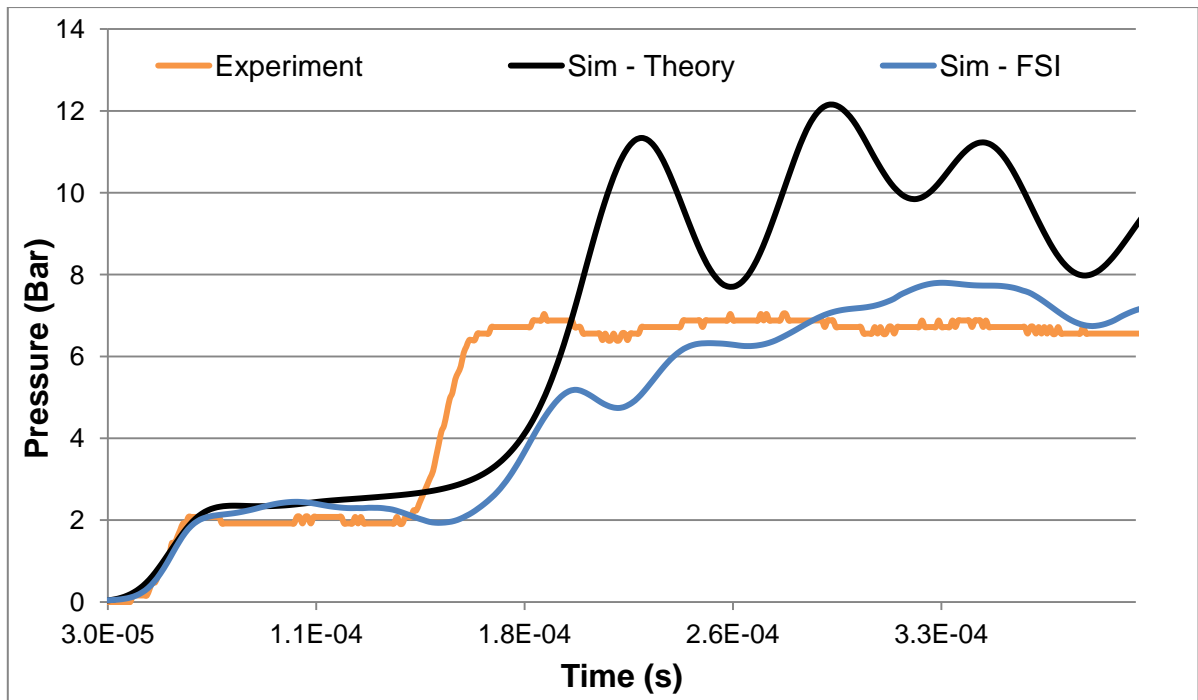


Figure 24: Reflected pressure for a driver pressure of 88 psi

The incident pressure profiles of the FSI simulation and the theoretical simulation are quite similar; however, the reflected profile of the FSI simulation clearly provides a better approximation of the experimental setup.

If the incident pressure region is the only point of interest, then it might be computationally more efficient to use the idealised gas column model.

Chapter 9: Conclusion

Simulations were conducted using Abaqus/Explicit in order to study the shock wave characteristics within a shock tube, the results of which were compared to those obtained using experiments.

The Simple Shock Tube Theory was confirmed to be inadequate in describing the experimental behaviour of thin, long shock tubes. This conforms to Duff's experimental observations at low pressures [1].

The study points out the negligible effect of user inputted material viscosity on the simulations.

Ultimately, a fluid structure interaction model that accounts for the transfer of stresses to the steel tube around the air column is determined to be the closest approximation of the experimental phenomena. However at lower pressures of 88 psi, the relative advantage of using such a model over a theoretical one is lost in the incident pressure region.

The intricacies of this model are studied and on further refinement, this model can be used to test the blast attenuation characteristics of specimens numerically for comparison with experimental tests.

Finally the findings of this project further validate Abaqus/Explicit's ability to accurately model and simulate a real life shock tube.

Chapter 10: Recommendations for Future Work

Immediate work that needs to be done includes conducting the FSI simulations at smaller mesh sizes in order to reduce the incident pressure overshoot that is observed. Smaller mesh sizes also reduce the width of the no slip layer that is created during the flow.

While it may be time consuming, it would be ideal to develop a model that involves no boundary conditions and relies solely on the Eulerian-Lagrangian interaction properties. This would require Eulerian element sizes of about 2 mm and corners that are more filleted. If such a simulation can be realised, it would provide the most accurate depiction of fluid structure interaction.

With regards to the experimental tests, it would be an added advantage if another pressure sensor could be bored into the circumference of the tube a few centimetres away from the end of the driven section. This would facilitate a more accurate approximation of the shock wave Mach number.

While the current model has approximately simulated the experimental setup, its real use lies in the testing of actual specimens computationally for verification with experimental data.

To start off, a simple Aluminium sheet with standard elastic plastic properties can be tested to determine the degree of blast attenuation or amplification caused by it. This could then be verified experimentally using a sheet of similar dimensions.

Once this is done, the same aluminium specimen can be modelled using the Mie-Gruneisen equation of state as outlined in [4] in order to observe the differences between the two material models.

On a longer time scale, it would be beneficial to model the behaviour of the shear thickening fluid or other materials under scrutiny and test them using the same FSI model. However, this might require extensive material testing and the creation of a user defined subroutine in case the material behaviour is not covered by the existing Abaqus material models.

References

- [1] Russel E. Duff, “Shock Tube Performance at Low Initial Pressure,” 1959
- [2] P. Carlucci, C. Mougeotte, and J. Huidi, “Validation of Abaqus Explicit – CEL for classes of problems of interest to the US Army,” *SIMULIA Customer Conference*, 2010
- [3] P.J.Petrie-Repar, and P.A. Jacobs, “A computational study of shock speeds in high-performance shock tubes,” *Shock Waves*, 1998
- [4] Tan, P., B. Lee, and C. Tsangalis, “FEA modelling prediction of the transmitted overpressure and particle acceleration within a frame subjected to shock tube blast loadings,” *18th World IMACS / MODSIM Congress*, 2009
- [5] Al-Falahi Amir, Yusoff M. Z, and Yusaf T., “Numerical Simulation of Inviscid transient Flows in Shock Tube and its Validations”, *Proceedings of World Academy of Science, Engineering and Technology*, 2008
- [6] J.D. Anderson, “Modern Compressible Flow,” 1982
- [7] University of Wisconsin, “Gas Dynamics Calculator,” *silver.neep.wisc.edu*
- [8] Steven P. Schneider, “Shock Tube Background,” 2009

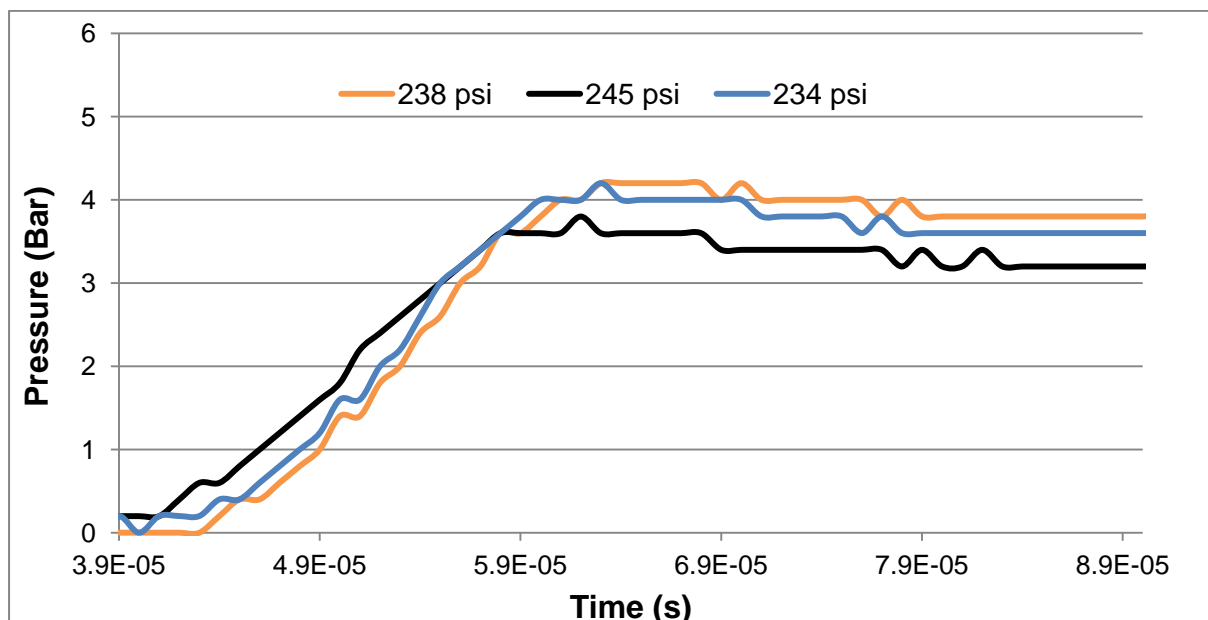
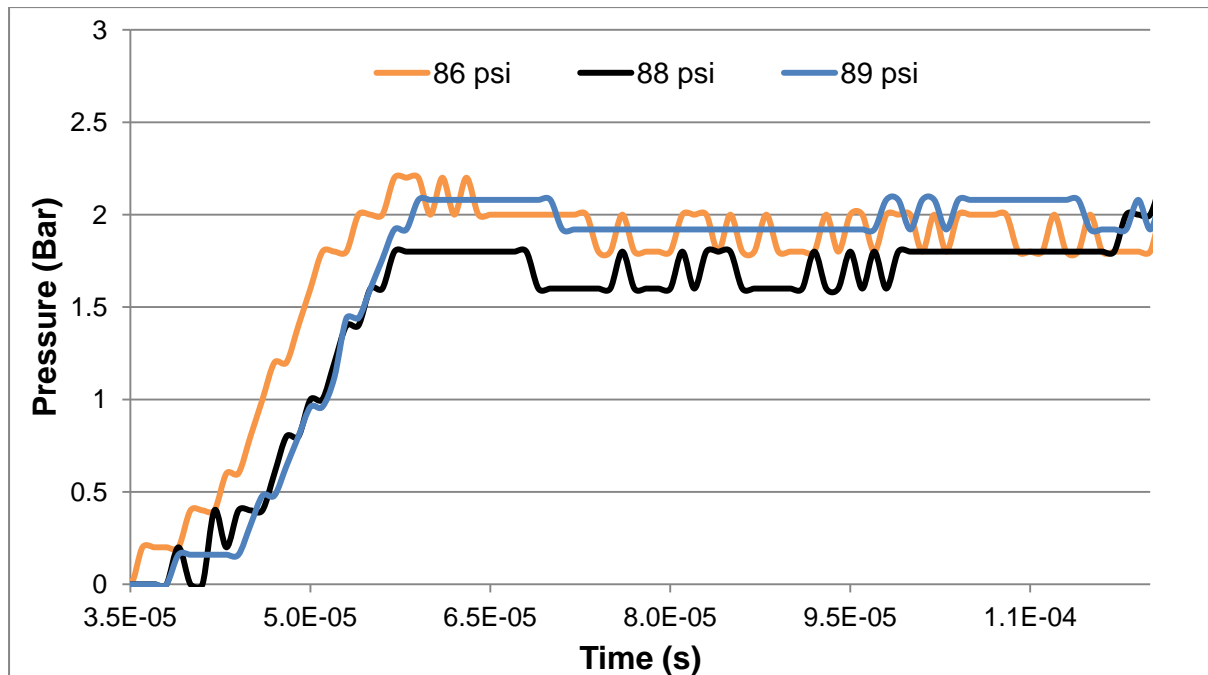
[9] Simulia, “Coupled Eulerian-Lagrangian Analysis with Abaqus/Explicit Lecture 04 - Techniques”

[10] Abaqus version 6.10 User Manual

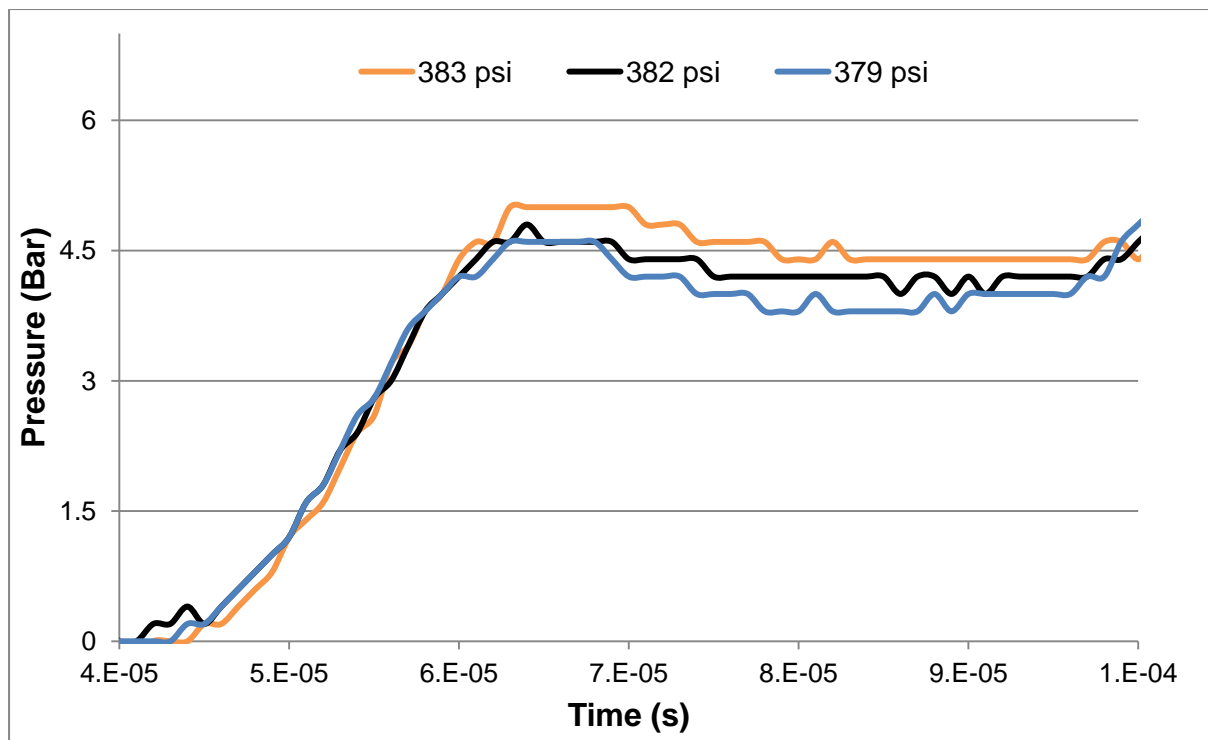
[11] Simulia, “Coupled Eulerian-Lagrangian Analysis with Abaqus/Explicit – web training,” *<http://www.simulia.com/services/training/wbtCEL/>*

Appendix I – Experimental Results

The graphs below show the experimental results for all three pressures of 88 psi, 238 psi and 382 psi respectively. The plots only cover the incident pressure region.



Incident Pressure profiles for bursting pressures of 88 psi (top) and 238 psi (bottom)



Incident pressure profile for bursting pressure of 382 psi

The graphs show a significantly higher amount of scatter for the 88 psi bursting pressure when compared with the 382 psi bursting pressure.

Appendix II – Fluid Structure Interaction Results

The graph below shows the FSI results for the 88 psi bursting pressure. Note that the pressure plot shows the distinct difference between the pressure plots at the centre of the shock wave and at the circumference of the tube. In fact the wall pressure plot shoots over the theoretical pressure before decreasing to the experimental curve. A finer mesh size could help reduce the degree of overshoot observed.

The pressure plot at the centre of the shock wave shows a better correlation with the experimental curve.

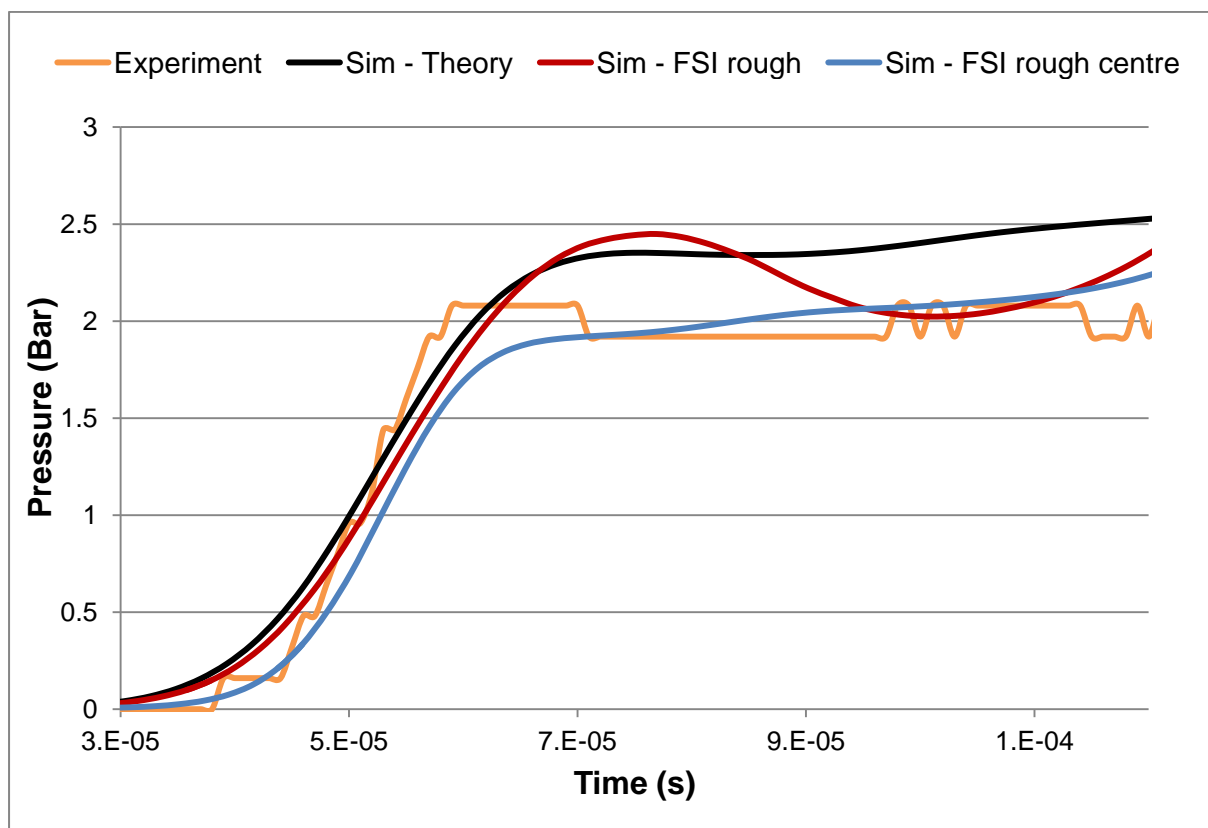
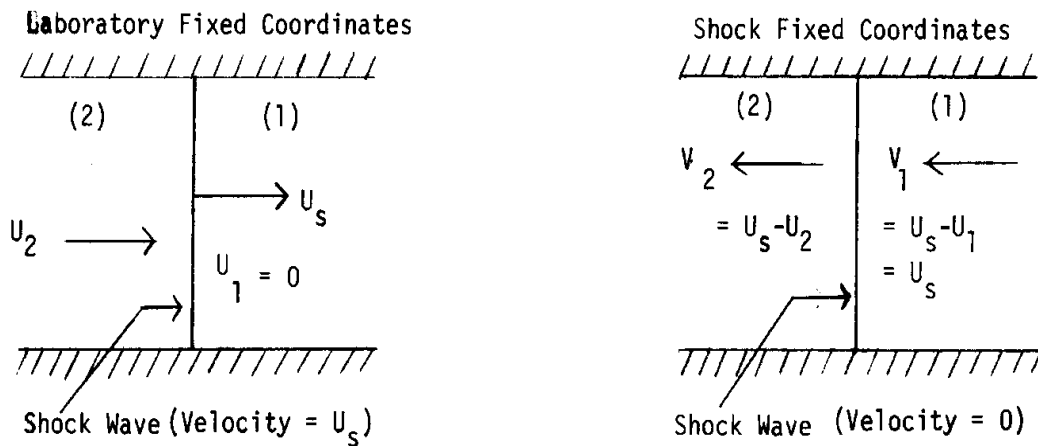


Figure showing the pressure plots at 88 psi. Experimental, theoretical and FSI pressures are plotted

Appendix III – The Simple Shock Tube Theory

The simple shock tube theory developed by Anderson [6] idealizes shock wave motion as a one dimensional, inviscid flow. In order to derive the static properties such as temperature and air before and after the shock wave, the moving shock wave is treated as a standing normal shock.



The shock wave shown in different coordinate systems. Figure courtesy Steven P. Schneider [8]

Using the fact that when a moving shock is converted to shock fixed coordinates it retains its static properties, the momentum, continuity and energy equations are solved to derive the following equations [8].

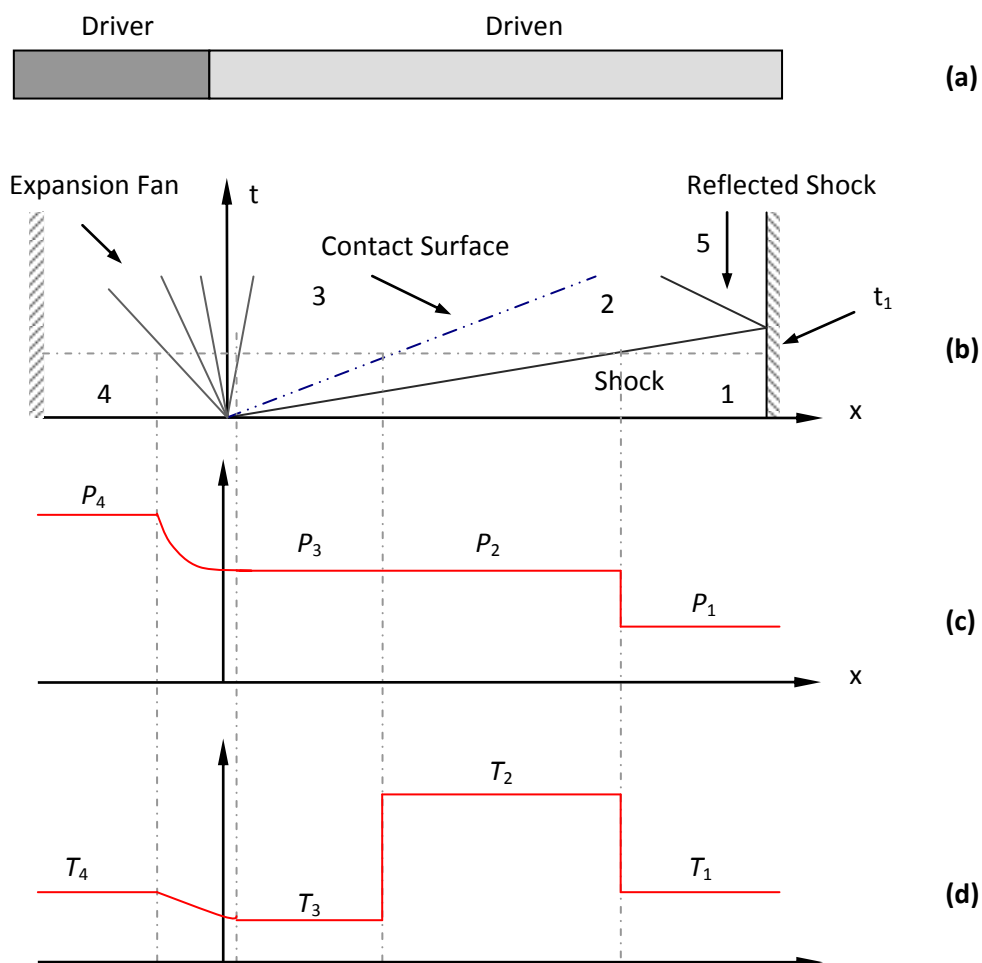
$$\frac{\rho_2}{\rho_1} = \frac{\frac{\gamma - 1}{\gamma + 1} + \frac{p_2}{p_1}}{\frac{\gamma - 1}{\gamma + 1} \frac{p_2}{p_1} + 1} \quad \text{and} \quad \frac{p_2}{p_1} = \frac{1 - \frac{\gamma - 1}{\gamma + 1} \frac{\rho_1}{\rho_2}}{\frac{\rho_1}{\rho_2} - \frac{\gamma - 1}{\gamma + 1}}$$

The subscripts 2 and 1 denote the parameters before and after the shock wave respectively.

These equations are collectively referred to as the Rankine-Hugoniot equations.

Using these equations and introducing the Mach number of the shock wave as a parameter, the equations outlined in chapter 5.1 are derived. Further details are provided by [8].

The idealized motion of the shock wave is summarized by the following diagram.



The figure outlines the driver and driven sections of the tube and the movement of the contact surface and shock front. Also shown are the pressure and temperature plots that one would expect using the idealized shock tube theory.

Appendix IV: Hourglass Controls

Hourglass controls are artificial numerical quantities introduced in Abaqus in order to provide more credible simulations. There are three main controls : displacement hourglass, linear bulk viscosity, and quadratic bulk viscosity.

Displacement hourglass is relevant for Lagrangian elements where the element deforms along with the material. This is especially important for reduced integration first order elements such as the C3D8R used to model the steel tube. In this brick element, there is only one integration point at the centroid of the element.

As the stresses and strains are calculated at this integration point, it is possible for the element to undergo deformation with no strain experienced by this integration point.



The figure shows the inability of the central integration point to detect the deformation and provide the requisite stiffness. Picture courtesy Abaqus/Explicit User Manual [10].

As shown by the figure above, the lines along the centre don't experience any change even though the edges do. In order to prevent this, Abaqus/Explicit provides hourglass controls in order to provide an artificial stiffness that resists such spurious deformation.

However, considering that the EC3D8R elements mentioned in this study contain gases and not solids, no such deformation occurs, rendering the hourglass control irrelevant.

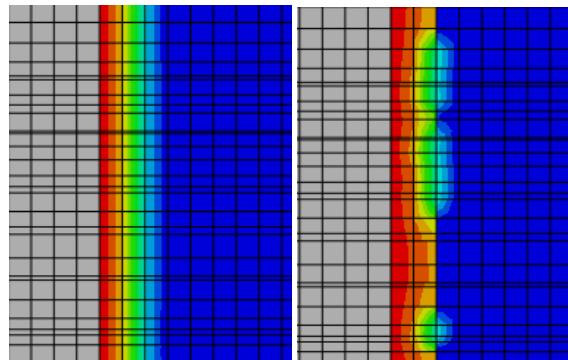
Quadratic bulk viscosity helps shear the pressure front across a number of elements in order to prevent an element from 'collapsing' under an extreme velocity gradient. This term is only

relevant when a continuum element is used and only when the stresses are compressive. It is hence switched off for the Eulerian mesh.

Bulk viscosity is introduced to dampen the ‘ringing’ (as defined by Abaqus) observed in the higher frequency terms by providing a resisting pressure that is a function of the volumetric strain in the element.

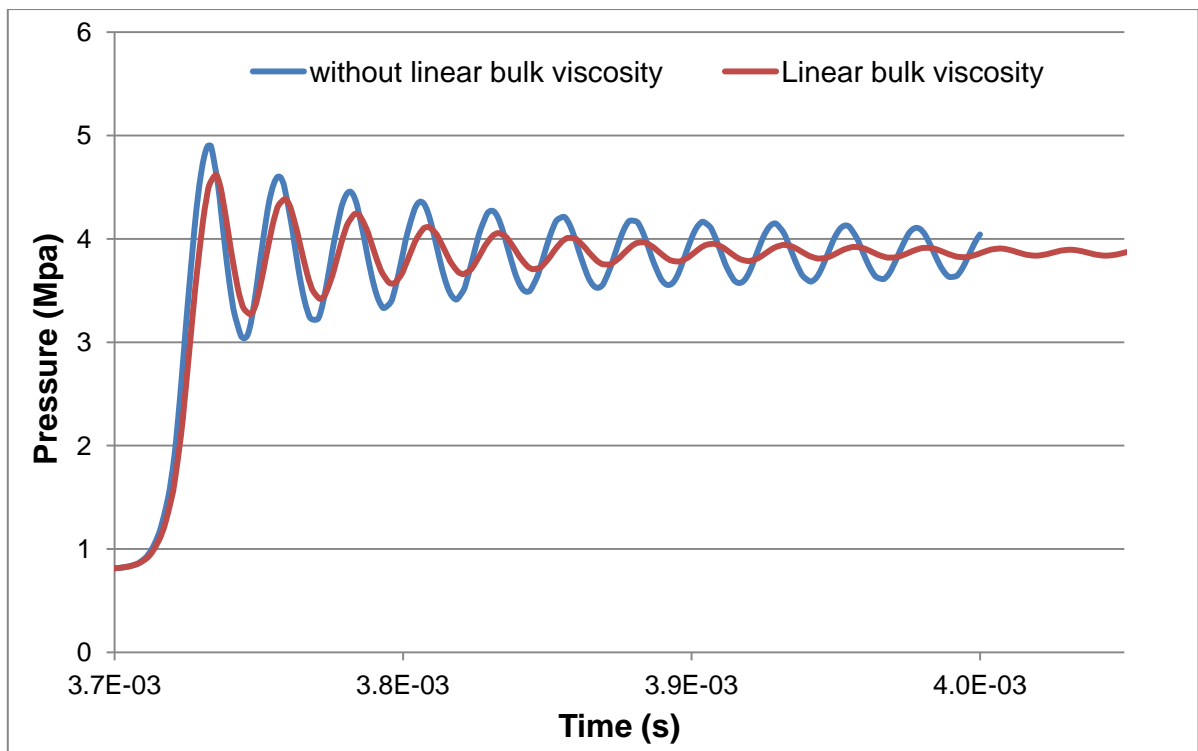
In order to study its effect, simulations using the gas column model were run with linear bulk viscosity enabled.

On analysing the contact surface between Helium and air, there appears to be a slightly non uniform dissipation in the simulation using linear bulk viscosity when compared with the simulation without it.



Helium contact surface without linear bulk viscosity on the left and with linear bulk viscosity on the right.

The introduction of the bulk viscosity term also reduces the amplitude of the oscillations seen in the reflected pressure region of the pressure plot shown in the figure below.



Dampening effect of linear bulk viscosity being shown.